IMPROVED BOUSSINESQ-TYPE EQUATIONS FOR HIGHLY-VARIABLE DEPTH *

JUAN CARLOS MUÑOZ GRAJALES † AND ANDRÉ NACHBIN‡

Abstract. Intermediate depth, Boussinesq-type modeling is used to generalize previously known results for surface water waves propagating over arbitrarly shaped topographies. The improved reduced wave model is obtained after studying how small changes in the linear dispersion relation (over a flat bottom) can become dramatically important in the presence of a highly-fluctuating topography. Numerical validation of the dispersive properties, regarding several possible truncations for the reduced models, are compared with the complete (non-truncated) linear potential theory model. Moreover, linear L^2 estimates are extended from the analysis of KdV-type models to include the improved Boussinesq systems in contrast with potential theory. Discrepancies observed among the different possible reduced models become even more important in the waveform inversion problem. The time reversal technique is used for recompressing a long fluctuating signal, representing a highly scattered wave that has propagated for very long distances. When properly backpropagated (through a numerical model), the scattered signal refocuses into a smooth profile representing the onset of the ocean's surface disturbance. Previous Boussinesq models underestimate the original disturbance's amplitude. The improved Boussinesq system agrees very well with the full potential theory predictions.

Key words. Boussinesq type models, highly variable coefficients, refocusing

AMS subject classifications. 76B07, 76B15, 35Q

1. Introduction. The physical applications for long wave interactions with topography range from coastal surface waves [22] to atmospheric flows over mountain ranges [3, 9]. Waves on the surface of an ideal fluid, under the force of gravity are governed by the Euler equations. Nevertheless in both engineering applications as well as laboratory scales, the full Euler equations appears more complex than necessary. Very often this system, for the entire fluid body, can be simplified to more tractable reduced surface models, when restricted to specific physical regimes. Under this modeling strategy Boussinesq-type equations, which include the lowest order terms regarding nonlinearity and dispersive effects, have been shown to provide an accurate description for wave evolution in coastal regions. The first set of equations valid for variable depth was derived by Peregrine [30] in 1967. The model is valid under the mild slope hypothesis.

Very recently there has been a great amount of research regarding additional modeling issues, namely in improving Boussinesq-type models as for example in [18, 19, 20, 29, 33, 21]. But all of these consider flat or slowly varying topographies. For very general topographies a terrain-following Boussinesq model was developed by Nachbin [28] in 2003. The model allows for multiply-valued topography profiles. This model was analyzed in [23, 24, 13, 15]. Existence and uniqueness for a variable coefficient Boussinesq system of equations was first given by Quintero and Muñoz in 2004 [32].

In the present paper we use ideas from Nwogu [29] and generalize them to the present scenario of highly-variable (*multiscale*) depth profiles. We show how small (higher order) changes in the linear dispersion relation (over a flat bottom) become

*This work was supported by Universidad del Valle, Cali,Colombia under the project No. 7660 and by CNPq/Brazil under Grant 300368/96-8.

†Universidad del Valle, A.A. 25360, Cali, Colombia (jcarlmz@yahoo.com). Fax (57)(2) 3393227.

‡Instituto de Matemática Pura e Aplicada, Est. D. Castorina 110, Jardim Botânico, Rio de Janeiro, RJ 22460-320, Brazil (nachbin@impa.br).

dramatically important in the presence of a highly-fluctuating topography. We present a linear dispersion analysis and validate the corresponding results both for a flat bottom and also in the presence of a variable propagation medium. In order to fully validate dispersive properties of several possible truncations, that can be made for these Boussinesq-type models, we compare them with the corresponding complete (non-truncated) model, namely linear potential theory. Moreover, in the appendix we extend linear L^2 estimates, deduced for KdV-type equations [5], in order to compare solutions of the improved Boussinesq systems with those of potential theory. For the numerical validation we use a new, highly efficient numerical scheme developed by Artiles and Nachbin [1, 2]. Discrepancies observed become even more important in the *waveform inversion problem* [31], an application for determining (for example) a tsunami's initial profile. Here we adopt the *time reversal technique* for recompressing a long fluctuating signal, representing a highly scattered wave that has propagated for very long distances. Time reversed recompression means that, if properly backpropagated (through a numerical model), the scattered signal will refocus into a smooth profile representing the original waveform, namely that which would have been observed at the onset of the ocean disturbance.

The paper is organized as follows. For completeness in section 2 we present an overview of the terrain-following formulation given in [28]. Hence it becomes clear how one can generate several different truncations regarding the different Boussinesq-type models. In section 3 we present improved systems, generalizing Nwogu's ideas [29], for highly variable topographies. We also present the dispersive properties for several different Boussinesq models. In section 4 we briefly describe the numerical methods developed by Wei and Kirby [34] and recently adapted by Muñoz and Nachbin [24] for the terrain-following Boussinesq model, together with a new efficient potential theory solver developed by Artiles and Nachbin [1]. In section 5 the dispersion properties are numerically validated and illustrated in the case of highly-variable depths. Finally in section 6 the waveform inversion problem is analysed for both Gaussian and solitary wave profiles and in section 7 we present our conclusions. Moreover, in the appendix L^2 estimates are deduced for comparing linear solutions of the (one parameter family of) Boussinesq equations with those of the potential theory equations.

2. Formulation and background of the problem. In this section we derive the family of governing equations adopted in this paper. These variable coefficient equations were introduced (without details) in a previous work by Quintero and Muñoz [32] where global existence and continuous dependence on parameters was demonstrated.

Consider the dimensionless form of the potential theory formulation for Euler's equations with a free surface and an impermeable bottom topography [35]:

$$\beta\,\phi_{xx} + \phi_{yy} = 0 \quad \text{for} \quad -H(x/\gamma) < y < \alpha\eta(x,t), \qquad -\infty < x < \infty, \tag{2.1}$$

subject to

$$\eta_t + \alpha\phi_x\eta_x - \frac{1}{\beta}\phi_y = 0, \tag{2.2}$$

$$\eta + \phi_t + \frac{\alpha}{2}\left(\phi_x^2 + \frac{1}{\beta}\phi_y^2\right) = 0 \tag{2.3}$$

at the free surface $y = \alpha\eta(x,t)$. The function $\phi(x,y,t)$ denotes the velocity potential, $\eta(x,t)$ the wave elevation measured with respect to the undisturbed free surface $y = 0$. The dimensionless parameters $\alpha = a_o/h_o$ and $\beta = h_o^2/\ell_p^2$ measure the strength of nonlinear and dispersive effects, respectively, and the parameter $\gamma = \ell/\ell_p$ measures the ratio inhomogeneities/wavelength. The typical amplitude is denoted by a_o, the typical depth by h_o and the typical wavelength by ℓ_p. The topography's horizontal length scale of variation is ℓ. In the potential theory model the fluid is assumed to be inviscid, incompressible and irrotational.

At the impermeable bottom the Neumann condition

$$\phi_y + \frac{\beta}{\gamma}\, H'(x/\gamma)\phi_x = 0 \tag{2.4}$$

is satisfied. We assume that the boundary at the bottom is described by the function $y = -H(x/\gamma)$ where

$$H(x/\gamma) \;=\; \begin{cases} 1 + n(x/\gamma) & \text{when } \; 0 < x < L \\ 1 & \text{when } \; x \le 0 \;\text{ or }\; x \ge L. \end{cases} \tag{2.5}$$

The bottom profile is described by the (possibly rapidly varying) function $n(x/\gamma)$. We point out that the topography is rapidly varying when $\gamma \ll 1$. The undisturbed depth is given by $y = -1$ and the topography can be of large amplitude provided that $|n| < 1$. The fluctuations n are not assumed to be small, nor continuous, nor slowly varying.

Next, in order to simplify the geometry of the problem and enable the asymptotical analysis of equations (2.1)-(2.5), we define a symmetric flow domain by reflecting the original one about the undisturbed free surface. In this symmetric domain we define curvilinear coordinates defined through the conformal mapping of this region. This strategy was already employed in [17] and [28]. For completeness we summarize the main ingredients of the asymptotic analysis in curvilinear coordinates. The symmetric domain is denoted by Ω_z where $z = x + i\sqrt{\beta}y$ and it can be considered as the conformal image of the strip Ω_w where $w = \xi + i\tilde{\zeta}$ with $|\tilde{\zeta}| \le \sqrt{\beta}$. Note that the topography is defined along the curve $\tilde{\zeta} \equiv -\sqrt{\beta}$. Then $z = x(\xi,\tilde{\zeta}) + i\ \sqrt{\beta}y(\xi,\tilde{\zeta}) = x(\xi,\tilde{\zeta}) + i\ \tilde{y}(\xi,\tilde{\zeta})$ where x and $\tilde{y}$ are a pair of harmonic functions on Ω_w. In figure 2.1, we present a scheme which explains the changes of variables to be introduced in the sequel.

The scaled water wave equations in the fixed orthogonal curvilinear coordinates $(\xi,\tilde{\zeta})$ are:

$$\phi_{\xi\xi} \;+\; \phi_{\tilde{\zeta}\tilde{\zeta}} \;=\; 0, \qquad\qquad -\sqrt{\beta} < \tilde{\zeta} < \alpha\sqrt{\beta}N(\xi,t), \tag{2.6}$$

with free surface conditions

$$|J|N_t + \alpha\phi_{\xi}N_{\xi} - \frac{1}{\sqrt{\beta}}\phi_{\tilde{\zeta}} = 0 \tag{2.7}$$

and

$$\phi_t + \eta + \frac{\alpha}{2|J|}\left(\phi_{\xi}^2 + \phi_{\tilde{\zeta}}^2\right) = 0 \tag{2.8}$$

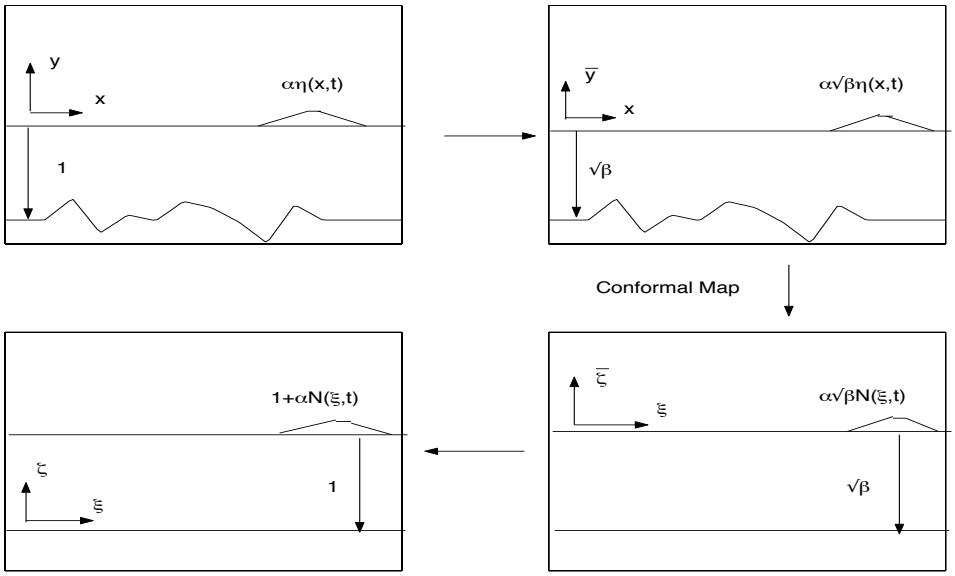

FIG. 2.1. *Schematic plot which explains the changes of variables introduced in the derivation of the extended Boussinesq equations. The conformal map transforming the rectangular coordinates* $(x, \tilde{y})$ *onto the curvilinear coordinates* $(\xi, \tilde{\zeta})$ *is indicated in this plot.*

at $\tilde{\zeta} = \alpha\sqrt{\beta}N(\xi, t)$. The bottom boundary condition (2.4) transforms into the trivial condition

$$\phi_{\tilde{\zeta}} = 0 \qquad \text{at} \quad \tilde{\zeta} = -\sqrt{\beta}. \tag{2.9}$$

The function $N(\xi, t)$ denotes the position of the free surface in the new coordinate system and $|J|$ denotes the Jacobian of the change of coordinates:

$$|J| = x_\xi \tilde{y}_{\tilde{\zeta}} - \tilde{y}_\xi x_{\tilde{\zeta}} = \tilde{y}_{\tilde{\zeta}}^2 + \tilde{y}_\xi^2.$$

At this point, it is convenient to let the origin of the curvilinear coordinate system be at the bottom and define $\tilde{\zeta} = \sqrt{\beta}(\zeta - 1)$. In the system of coordinates (ξ, ζ), equations (2.6)-(2.9) transform into

$$\beta\phi_{\xi\xi} \; + \; \phi_{\zeta\zeta} \; = \; 0, \qquad \text{at} \quad 0 < \zeta < 1 + \alpha N(\xi, t), \tag{2.10}$$

with free surface conditions

$$|J|N_t + \alpha\phi_\xi N_\xi - \frac{1}{\beta}\phi_\zeta = 0, \tag{2.11}$$

$$\eta + \phi_t + \frac{\alpha}{2|J|}\left(\phi_\xi^2 + \frac{1}{\beta}\phi_\zeta^2\right) = 0 \tag{2.12}$$

at $\zeta = 1 + \alpha N(\xi, t)$ and

$$\phi_\zeta = 0 \qquad \text{at} \quad \zeta = 0. \tag{2.13}$$

As in Whitham [35], consider a power series expansion near the bottom of the channel in the form

$$\phi(\xi,\zeta,t)=\sum_{n=0}^{\infty}\zeta^n\ f_n(\xi,t). \tag{2.14}$$

Asymptotic analysis will be performed at the level of the equations in terms of the small parameters α and β.

By substituting this expression in the scaled Laplace equation (2.10) and using the Neumann condition (2.13) at the bottom we can express the potential as a power expansion in β

$$\phi(\xi,\zeta,t)=\sum_{n=0}^{\infty}\frac{(-\beta)^n}{(2n)!}\zeta^{2n}\frac{\partial^{2n}f(\xi,t)}{\partial\xi^{2n}} \tag{2.15}$$

where, for simplicity, $f(\xi,t)=f_0(\xi,t)$.

Now using that at the smooth free surface $\tilde{\zeta}_{FS}=\alpha\sqrt{\beta}N(\xi,t)$ the Jacobian is

$$|J|(\xi,t)=\tilde{y}^2_{\xi}(\xi,\tilde{\zeta}_{FS})+\tilde{y}^2_{\tilde{\zeta}}(\xi,\tilde{\zeta}_{FS}),$$

and the Taylor polynomial formula leads to

$$|J|(\xi,t)=\tilde{y}^2_{\tilde{\zeta}}(\xi,0)+\alpha^2R_J(\xi,\tilde{\zeta}_M)=M(\xi)^2+O(\alpha^2),\quad 0<|\tilde{\zeta}_M|<|\tilde{\zeta}_{FS}|. \tag{2.16}$$

The metric term $M(\xi)$ is defined below. Thus, the Jacobian can be well approximated by an $O(1)$ time independent coefficient. The time dependent correction term is $O(\alpha^2)$ due to the fact that the curvilinear coordinate system is symmetric about $\tilde{y}=\tilde{\zeta}=0$. There are no $O(\alpha)$ terms. For the same reason, approximating $\tilde{\zeta}(x,\tilde{y}_{FS})$ in $\tilde{y}$ leads to

$$N(\xi,t)=\frac{1}{M(\xi)}\eta(x(\xi),t)+\alpha^2\beta R_N(\xi,\tilde{y}_M),\quad 0<|\tilde{y}_M|<|\tilde{y}_{FS}|, \tag{2.17}$$

and we establish a relation between the free surface representation in curvilinear coordinates ($N(\xi,t)$) and in cartesian coordinates ($\eta(x,t)$).

At the undisturbed level we define the **variable free surface coefficient** [28]

$$M(\xi)\equiv\tilde{y}_{\tilde{\zeta}}(\xi,0)=1+m(\xi)$$

where

$$m(\xi;\sqrt{\beta},\gamma)\equiv\frac{\pi}{4\sqrt{\beta}}\int_{-\infty}^{\infty}\frac{n(x(\xi_0,-\sqrt{\beta})/\gamma)}{cosh^2\frac{\pi}{2\sqrt{\beta}}(\xi_0-\xi)}d\xi_0\ =\ (K*(n\circ x))(\xi). \tag{2.18}$$

Recall that the square of the metric term $M(\xi)$ is the leading order term of the Jacobian. Note also that the coefficient $M(\xi)$ is smooth even when the function describing the bottom is discontinuous or non differentiable. Moreover the metric coefficient is time independent and becomes identically one in the case of a constant depth. These features are important when implementing a numerical solver for the Boussinesq formulation.

Introducing the approximations (2.16), (2.17) in the equations (2.10)-(2.13), it gives

$$\beta\phi_{\xi\xi}\ +\ \phi_{\zeta\zeta}\ =\ 0,\qquad \text{at}\ \ 0<\zeta<1+\alpha\frac{\eta(\xi,t)}{M}, \tag{2.19}$$

with free surface conditions

$$M\eta_t + \alpha\phi_\xi \left(\frac{\eta}{M}\right)_\xi - \frac{1}{\beta}\phi_\zeta = 0, \tag{2.20}$$

$$\eta + \phi_t + \frac{\alpha}{2M^2}\left(\phi_\xi^2 + \frac{1}{\beta}\phi_\zeta^2\right) = 0 \tag{2.21}$$

at $\zeta = 1 + \alpha\frac{\eta(\xi,t)}{M}$ and

$$\phi_\zeta = 0 \qquad \text{at } \zeta = 0. \tag{2.22}$$

Using the power series expansion for the potential the free surface conditions (2.20)-(2.21) can be further approximated as

$$\eta + f_t - \frac{\beta}{2}f_{\xi\xi t} + \frac{\alpha}{2M^2(\xi)}f_\xi^2 = O(\alpha\beta, \beta^2), \tag{2.23}$$

$$M(\xi)\ \eta_t + \left[\left(1 + \frac{\alpha}{M(\xi)}\eta\right) f_\xi\right]_\xi - \frac{\beta}{6}f_{\xi\xi\xi\xi} = O(\alpha^2, \alpha\beta, \beta^2). \tag{2.24}$$

Remark that the variable coefficients in the system above are time independent and depend only on $\tilde{y}_{\tilde{\zeta}}(\xi, 0)$. This is a consequence of equations (2.16)-(2.17). Moreover, the transversal curvilinear coordinate ζ does not appear in the equations above.

In [28] it is shown that equations (2.23)-(2.24) lead to the **terrain-following system**

$$M(\xi)\eta_t + \left[\left(1 + \frac{\alpha\ \eta}{M(\xi)}\right) U_o\right]_\xi = 0, \tag{2.25}$$

$$U_{o,t} + \eta_\xi + \alpha\left(\frac{U_o^2}{2M^2(\xi)}\right)_\xi - \frac{\beta}{3}U_{o,\xi\xi t} = 0, \tag{2.26}$$

where U_o is the depth averaged velocity

$$U_o(\xi, t) = \frac{1}{\zeta_{FS}}\int_0^{\zeta_{FS}} \phi_\xi(\xi, \zeta, t)d\zeta. \tag{2.27}$$

As pointed out in Nachbin [28] these are weighted averages along ($\xi \equiv$constant)-curves connecting the undisturbed free surface to the topography (c.f. figure 2.2). It turns out that the conformal mapping gives more weight near the free surface, than to the regions in the deep valleys, where the topography is rapidly varying.

3. Improved Boussinesq systems. In the present work, instead of using the depth averaged velocity, we will express the evolution equations in terms of the fluid velocity measured at **an intermediate depth**, say at $\zeta = Z_0(\xi)$, with $u(\xi, t) = \phi_\xi(\xi, Z_0(\xi), t)$, where $0 < Z_0(\xi) < 1$. This idea was already applied by Nwogu [29] to obtain a formally equivalent Boussinesq approximation, in the case where the depth is slow-varying. The purpose was to improve the dispersive characteristics of the resulting reduced model. Recall that we are interested in the case where the topography dependent coefficient $M(\xi)$ is allowed to (also) vary on a fast scale denoted

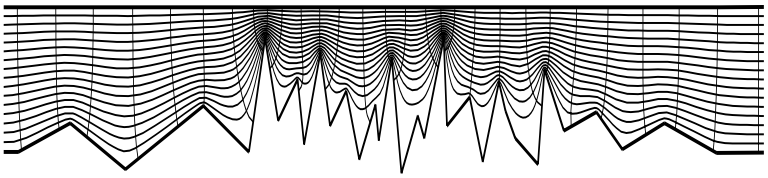

FIG. 2.2. *Multiscale topography with the $\xi - \zeta$ curvilinear coordinate system.*

by ℓ [15, 13, 14, 16, 23, 24, 28]. In the sequel we will show how, by using curvilinear coordinates, we are able to extend Nwogu's strategy to more general topography profiles.

Differentiating equation (2.15) with respect to ξ and evaluating at $\zeta = Z_0(\xi)$, we find

$$u(\xi,t) = \phi_\xi(\xi, Z_0, t) = f_\xi - \frac{\beta}{2} Z_0^2 f_{\xi\xi\xi} + O(\beta^2) = \tilde{u} - \frac{\beta}{2} Z_0^2 \tilde{u}_{\xi\xi} + O(\beta^2), \tag{3.1}$$

where for simplicity, we let $\tilde{u} = \tilde{u}(\xi,t) = f_\xi(\xi,t)$ be the "slip velocity" along the bottom of the channel. As a consequence,

$$\tilde{u} = u(\xi,t) + \frac{\beta}{2} Z_0^2 \tilde{u}_{\xi\xi} + O(\beta^2). \tag{3.2}$$

Substituting the expression for $\tilde{u}$ (given by the equation above) into equations (2.23)-(2.24) and retaining only terms up to $O(\alpha)$, $O(\beta)$, we arrive at the system

$$M(\xi)\eta_t + \left[\left(1 + \frac{\alpha\,\eta}{M(\xi)}\right) u\right]_\xi + \frac{\beta}{2}\left[\left(Z_0^2 - \frac{1}{3}\right) u_{\xi\xi}\right]_\xi = 0, \tag{3.3}$$

$$u_t + \eta_\xi + \alpha\left(\frac{u^2}{2M^2(\xi)}\right)_\xi + \frac{\beta}{2}(Z_0^2 - 1) u_{\xi\xi t} = 0. \tag{3.4}$$

An interesting observation is that the system above reduces to the terrain-following system (2.25)-(2.26) when we set $Z_0 = \sqrt{1/3}$. Namely at this intermediate depth the system is exactly the same as using the (ζ) depth-averaged velocity.

Several Boussinesq formulations can be derived from equations (3.3)-(3.4) depending on where the terrain-following velocity (ϕ_ξ) is monitored. In particular, by letting $Z_0 = \sqrt{2/3}$, system (3.3)-(3.4) reads

$$M(\xi)\eta_t + \left[\left(1 + \frac{\alpha\,\eta}{M(\xi)}\right) u\right]_\xi + \frac{\beta}{6} u_{\xi\xi\xi} = 0, \tag{3.5}$$

$$u_t + \eta_\xi + \alpha\left(\frac{u^2}{2M^2(\xi)}\right)_\xi - \frac{\beta}{6} u_{\xi\xi t} = 0. \tag{3.6}$$

Equation (3.5) implies in

$$u_\xi(\xi,t) = -M(\xi)\eta_t + O(\alpha,\beta). \tag{3.7}$$

By putting this relationship into system (3.5)-(3.6), and retaining only terms of order $O(\alpha, \beta)$, we obtain the model

$$(M(\xi)\eta)_t + \left[\left(1 + \frac{\alpha\ \eta}{M(\xi)}\right) u\right]_\xi - \frac{\beta}{6}(M(\xi)\eta)_{t\xi\xi} = 0, \tag{3.8}$$

$$u_t + \eta_\xi + \alpha\left(\frac{u^2}{2M^2(\xi)}\right)_\xi - \frac{\beta}{6}u_{\xi\xi t} = 0. \tag{3.9}$$

System (3.8)-(3.9) was presented by Quintero and Muñoz in [32]. The main property of this particular Boussinesq formulation is the existence of a conserved energy-type functional which enables the use of classical tools to demonstrate the global existence of its solutions [32]. We remark that the existence of this conserved quantity is unclear for the Boussinesq model (2.25)-(2.26). Of equal importance is the presence of symmetric dispersive terms in both equations of the system (3.8)-(3.9), expressed through the operator $\partial_t - \beta/6\partial_{\xi\xi t}$. This operator can be inverted [32] and the system cast into an integro-differential form, so that the fixed point principle can be applied in order to establish local existence of solutions.

Note that the dispersive terms of the model above are modified when we change the level at which the fluid velocity u is measured, i.e. the parameter Z_0. We remark that this degree of freedom (to select the parameter Z_0) allows us to match the linear dispersion relation, corresponding to the Boussinesq approximation (3.3)-(3.4), with that of the original potential theory equation (2.19)-(2.22) up to a higher order. This will be explained in section 3.1.

Furthermore, note that all variable coefficients in the model are smooth even when the physical topography profile is described by a discontinuous or even a multi-valued function. We point out that Nwogu [29] obtained a set of equations with dispersive terms similar to those in system (3.3)-(3.4) However, the applicability of Nwogu's formulation is restricted to slowly-varying bottom profiles, which is a common feature of other Boussinesq-type formulations, as for instance [30, 19, 20, 33, 36, 18]. The reason is that in cartesian coordinates the neglected terms of order $O(\alpha^2, \alpha\beta, \beta^2)$ in the Boussinesq model turn out to be large when the detailed features of the topography are small compared to the typical wavelength [17].

In contrast, in the present Boussinesq formulation (3.3)-(3.4), the neglected terms of order $O(\alpha^2, \alpha\beta, \beta^2)$ remain small **even when the topography is rapidly varying**. This is due to the use of terrain-following (curvilinear) coordinates [28]. Thus, we expect that the solutions of equations (2.19)-(2.22) and system (3.3)-(3.4) coincide with good accuracy even when dispersion is significant. The agreement between the two models, in the presence of nontrivial dispersion, is demonstrated rigorously in appendix A in the case where the depth is constant.

When the bottom is described by a complicated function, we can not prove this fact but the numerical experiments, to be presented in the following section, will provide strong numerical evidence on this regard within the range $0 < \beta < 0.05$, $\alpha = 0.001$. To be specific, in a laboratory scale this regime is such that for example, if $h_o = 10\ mt$ (characteristic depth), $a_o = 0.01\ mt$, (characteristic wave amplitude) and the typical pulse width is $\ell_p \approx 44.7214\ mt$. In the ocean these are *at least* scaled by a factor of 100. For example a tsunami has a few meters of amplitude and several kilometers of length. It can be generated in regions one thousand meters deep.

3.1. Linear dispersive properties. To perform an analysis regarding the dispersive terms in equations (3.3)-(3.4) it is sufficient to consider the intermediate depth

Z_0 to be a constant.

It is important to remark what is expected from the asymptotically simplified Boussinesq model (3.3)-(3.4). It would be desirable that its solution approximates, in some sense, the solution of the original potential theory equations (2.19)-(2.22), provided that $0 < \alpha << 1$, $0 < \beta << 1$. Within this regime the high-order terms $O(\alpha^2, \alpha\beta, \beta^2)$ are expected to be negligible with respect to the first order terms retained in the Boussinesq model (3.3)-(3.4).

The analytical, dispersion relation, consistency between the Boussinesq system (3.3)-(3.4) and the potential formulation of the Euler equations (2.19)-(2.22) is a necessary condition so that the new model is able to capture the same (long wave) physical phenomena as the original fluid equations.

To start, consider the linear dispersion relation with the phase velocity

$$C^2 = \frac{\omega^2}{k^2} = \frac{1-(\beta/2)(Z_0^2-\frac{1}{3})k^2}{1-(\beta/2)(Z_0^2-1)k^2} \tag{3.10}$$

for model (3.3)-(3.4). Also we have the phase velocity for Airy waves given by

$$\begin{aligned} C^2_{\text{Airy}} = \frac{\omega^2}{k^2} &= \frac{1}{\sqrt{\beta}k} tanh(\sqrt{\beta}k) \\ &\approx 1 - \frac{1}{3}(\sqrt{\beta}k)^2 + \frac{2}{15}(\sqrt{\beta}k)^4 - \frac{17}{315}(\sqrt{\beta}k)^6 + O((\sqrt{\beta}k)^8), \end{aligned} \tag{3.11}$$

corresponding to equations (2.19)-(2.22). The approximations above correspond to the Taylor series expansions for $\sqrt{\beta}k$ small. Observe that, according to equation (3.10), the velocity of propagation of solutions to models (3.3)-(3.4) and (2.19)-(2.22) depend on the wave number k, indicating their dispersive nature. Furthermore the phase speed is affected by depth Z_0 selected in the Boussinesq model. We remark that the dispersion relation (3.10) corresponds to a Padé approximation of the exact dispersion relation (3.11).

As mentioned above, the interesting point here is that we can use this degree of freedom (by selecting the parameter Z_0) in order to match the Taylor series expansion of the dispersion relation (3.11) up to terms of $O((\sqrt{\beta}k)^4)$. This will be shown below. By using a particular value of the intermediate depth variable Z_0 we can decrease the errors in the phase velocity introduced when the high-order terms $O(\alpha^2, \alpha\beta, \beta^2)$ are neglected in the asymptotic analysis used to derive the equations (3.3)-(3.4).

Recall that in constant depth, this fact can be established rigorously by using the Fourier transform technique. This is accomplished in appendix A where we show that the difference in L^2–norm of the solutions of models (2.19)-(2.22) and the Boussinesq system (3.3)-(3.4) with $\alpha = 0$ (linear regime) and constant depth ($M \equiv 1$) is smallest when $Z_0 = \sqrt{1/5}$ within a time interval which tends to infinity when $\beta \to 0$. The analysis extends that presented in [5] which considered KdV-type models. For this value of the parameter Z_0, the dispersion relation (3.10) transforms into

$$\begin{aligned} \frac{\omega^2}{k^2} &= \frac{1+(\beta/15)k^2}{1+2(\beta/5)k^2} \\ &\approx 1 - \frac{1}{3}(\sqrt{\beta}k)^2 + \frac{2}{15}(\sqrt{\beta}k)^4 - \frac{4}{75}(\sqrt{\beta}k)^6 + O((\sqrt{\beta}k)^8). \end{aligned} \tag{3.12}$$

This result is beyond expected since the Boussinesq model is only accurate up to order $O(\alpha, \beta)$. Thus, we get a significant improvement in accuracy of the dispersion

relation of the Boussinesq approximation (3.3)-(3.4), in contrast to system (2.25)-(2.26) which is based on the depth averaged velocity. We remark that the linear dispersion corresponding to the terrain-following system (2.25)-(2.26) is only accurate up to order $O(\beta)$.

However, we can obtain an optimal value of the depth parameter Z_0, by minimizing the relative error of the phase velocity for instance, over the frequency interval $0 < \sqrt{\beta}k < 5$. The result of this process is the value $Z_0 = 0.469$ [29]. It gives a maximum error of 6 % for the entire range. In contrast, for the terrain-following system (2.25)-(2.26), we obtain a maximum relative error in the same interval of 15 %. This is shown in figure 3.1 where we compare the dispersion relations for the terrain-following system (2.25)-(2.26), with the one for formulation (3.3)-(3.4) having either $Z_0 = \sqrt{1/5}$ or $Z_0 = 0.469$. The relative error is computed with respect to the linear potential equations (2.19)-(2.22).

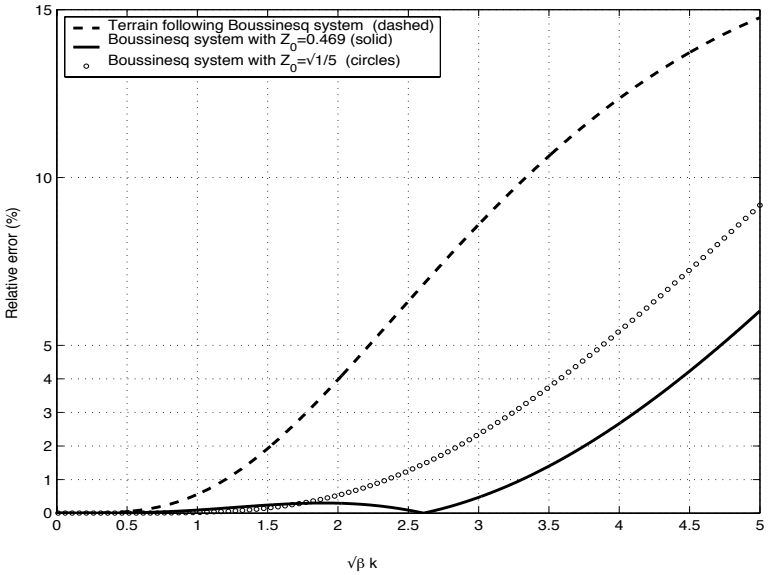

FIG. 3.1. *Relative error of the phase velocity as a function of* $\sqrt{\beta}k$ *for the Boussinesq-type system (3.3)-(3.4) with* $Z_0 = \sqrt{1/3}$ *(the terrain-following system),* $Z_0 = 0.469$ *and* $Z_0 = \sqrt{1/5}$.

4. Numerical schemes. In this section we want to provide numerical evidence regarding the dispersion analysis presented above and also explore the differences between the various (variable coefficient) Boussinesq models, namely when in the presence of rapidly varying topographies.

4.1. Numerical scheme for the Boussinesq models. For completeness we present the numerical scheme employed in computing the solutions to the one parameter family of Boussinesq systems (3.3)-(3.4). This scheme is basically the same as that developed by Wei and Kirby [34] and which we adapted in [24]. For simplicity, let

$$g(\xi) = \frac{1}{2}(Z_0^2(\xi) - 1).$$

First we rewrite the system in a more convenient way, as

$$\begin{aligned} \eta_t &= E(\eta, u), \\ V_t &= F(\eta, u), \end{aligned} \tag{4.1}$$

where

$$\begin{aligned} E(\eta,u) &= -\frac{1}{M(\xi)}\left(\left(1+\frac{\alpha\eta}{M(\xi)}\right)u\right)_\xi + \frac{\beta}{M(\xi)}((g(\xi)+1/3)u_{\xi\xi})_\xi, \\ F(\eta,u) &= -\eta_\xi - \frac{\alpha}{2}\left(\frac{u^2}{M(\xi)^2}\right)_\xi. \end{aligned} \tag{4.2}$$

The intermediate variable V is defined as

$$V = u - \beta g(\xi) u_{\xi\xi}.$$

We now approximate the solution of system (4.1) by using a high-order predictor-corrector solver. The space-time domain $\{\xi \in [\xi_1, \xi_J]\ ,\ t \geq 0\}$ will be discretized by $\xi_j = \xi_1 + (j-1)\Delta\xi,\ 1 \leq j \leq J$ and $t_n = (n-1)\Delta t,\ 1 \leq n \leq N_0$, respectively. The discretizations of the variables u, η, V will be denoted by u_j^n, η_j^n, V_j^n. As mentioned above this strategy is basically the same as that presented in [24], the difference being that the Sturm-Liouville type problem, for inverting the change of variables from V back to u, has the new coefficient $g(\xi)$.

As suggested in [34] we use a third-order explicit Adams-Bashforth solver to produce a predicted value for (V, η) and then a fourth-order implicit Adams-Moulton scheme is applied to obtain a corrected solution. The **predictor** is given by

$$\begin{aligned} \eta_j^{n+1} &= \eta_j^n + \frac{\Delta t}{12}(23E_j^n - 16E_j^{n-1} + 5E_j^{n-2}), \\ V_j^{n+1} &= V_j^n + \frac{\Delta t}{12}(23F_j^n - 16F_j^{n-1} + 5F_j^{n-2}). \end{aligned} \tag{4.3}$$

The notation $E_j^n = E(\eta_j^n, u_j^n)$ and $F_j^n = F(\eta_j^n, u_j^n)$ is used. The first-order derivatives in equation (4.2) and $u_{\xi\xi\xi}$ are approximated by appropriate differences schemes [24]. Recall that for evaluating the fluid velocity u_j^{n+1} we must solve the (spatial) ordinary differential equation

$$u - \beta g(\xi) u_{\xi\xi} = V, \tag{4.4}$$

which is forced by the known left handside V_j^{n+1}. The second derivative in equation (4.4) is discretized by a centered approximation giving rise to a tridiagonal system of algebraic equations which is solved very efficiently. We remark that this system's matrix is constant in time and thus only one LU decomposition must be performed at the starting point.

When the boundary values u_1^{n+1} and u_J^{n+1} and η_1^{n+1} and η_J^{n+1} are required, we use the linear radiation conditions (B. Engquist and A. Majda [10])

$$\begin{aligned} u_t - u_\xi &= 0, \quad \text{at} \ \ \xi = \xi_1, \\ u_t + u_\xi &= 0, \quad \text{at} \ \ \xi = \xi_J, \end{aligned} \tag{4.5}$$

where ξ_1 and ξ_J denote the left and right ends of the computational domain. Analogous conditions are applied on the function η. Conditions above play the role of absorbing the waves arriving at the boundaries of the computational domain. This allows us to perform numerical simulations without introducing a too long computational spatial domain. These conditions work well for small amplitude waves propagating in the linear regime in the absence of a topography. Therefore at the extremes of our computational domain the channel has a short flat bottom region.

Once the predicted values η_j^{n+1}, u_j^{n+1} are obtained we compute E_j^{n+1}, F_j^{n+1} from equations (4.2). The **corrected values** are calculated from

$$\begin{aligned} \eta_j^{n+1} &= \eta_j^n + \frac{\Delta t}{24}(9E_j^{n+1} + 19E_j^n - 5E_j^{n-1} + E_j^{n-2}), \\ V_j^{n+1} &= V_j^n + \frac{\Delta t}{24}(9F_j^{n+1} + 19F_j^n - 5F_j^{n-1} + F_j^{n-2}), \end{aligned} \tag{4.6}$$

where the quantities at level $n+1$ are computed iteratively by using the predicted approximation as the initial guess. The new u_j^{n+1} is computed from V_j^{n+1} as in the predictor step. We stop the iteration process when the relative error between two successive corrected values η^{n+1}, u^{n+1} and $\eta^{(n+1)^*}$, $u^{(n+1)^*}$ are smaller than a given tolerance.

To verify the stability and the accuracy of this numerical scheme we perform a simulation with constant depth, taking alternatively $Z_0 = \sqrt{1/5}$, $Z_0 = 0.469$.

Adapting the strategy described in [34] an approximate solitary wave solution for system (3.3)-(3.4) can be written as

$$\begin{aligned} \eta(\xi,t) &= A_1 sech^2(B(\xi - Ct - \xi_o)) + A_2 sech^4(B(\xi - Ct - \xi_o)), \\ u(\xi,t) &= A sech^2(B(\xi - Ct - \xi_o)), \end{aligned} \tag{4.7}$$

where

$$A_1 = \frac{C^2-1}{\frac{3}{2}\alpha(Z_0^2 - 1/3 - (Z_0^2-1)C^2)}, \quad A_2 = -\frac{(C^2-1)^2(\frac{1}{2}(Z_0^2-1/3) + (Z_0^2-1)C^2)}{\alpha C^2(Z_0^2 - \frac{1}{3}) - (Z_0^2-1)C^2}$$

$$B = \left\{ \frac{C^2-1}{2\beta(Z_0^2 - 1/3 - (Z_0^2-1)C^2)} \right\}^{1/2}, \quad A = \frac{C^2-1}{\alpha C}.$$

The parameter ξ_o indicates the location of the solitary wave at $t = 0$. The constant C is the wave velocity and it is calculated from the equation

$$2(Z_0^2-1)C^6 - ((3+2\alpha)(Z_0^2-1) + \frac{2}{3})C^4 + 2\alpha(Z_0^2 - \frac{1}{3})C^2 + Z_0^2 - \frac{1}{3} = 0. \tag{4.8}$$

Observe that the wave speed and the amplitude of the wave are connected. We point out that (4.7) corresponds to an exact solitary wave for the Benney-Luke type equation

$$\phi_{tt} - \phi_{\xi\xi} + \alpha(2\phi_\xi\phi_{\xi t} + \phi_t\phi_{\xi\xi}) - \beta(\frac{Z_0^2 - 1/3}{2}\phi_{\xi\xi\xi\xi} - \frac{Z_0^2-1}{2}\phi_{\xi\xi tt}) = 0,$$

which is formally equivalent to system (3.3)-(3.4) (with $u = \phi_\xi$) up to order $O(\alpha, \beta)$.

We now perfom a numerical experiment. When $\alpha = \beta = 0.03$, and $Z_0 = \sqrt{1/5}$ or $Z_0 = 0.469$, the wave speed (computed from (4.8)) is approximately $C \approx 1.01485$.

In the simulation the discretization parameters used were $\Delta\xi = 0.0333$, $\Delta t = 0.0267$ and the computational domain is taken as [0,100]. In these experiments, we observe that the solitary wave preserves its shape after propagating over a distance of approximately 13 times its effective width ($\ell \approx 6$). There is no indication of numerical attenuation nor spurious dispersion. The solitary wave speed coincides with good accuracy with the speed of the numerical solitary solution. This was systematically observed in several numerical experiments with different values of the parameters α, β and of the intermediate depth Z_0 in system (3.3)-(3.4). We remark that the dispersion and nonlinearity values $\alpha = \beta = 0.03$ are not negligible [23, 24] in this problem. Thus, we conclude that the numerical scheme is describing very well both nonlinear and dispersive effects present in the (one parameter family) Boussinesq models (3.3)-(3.4).

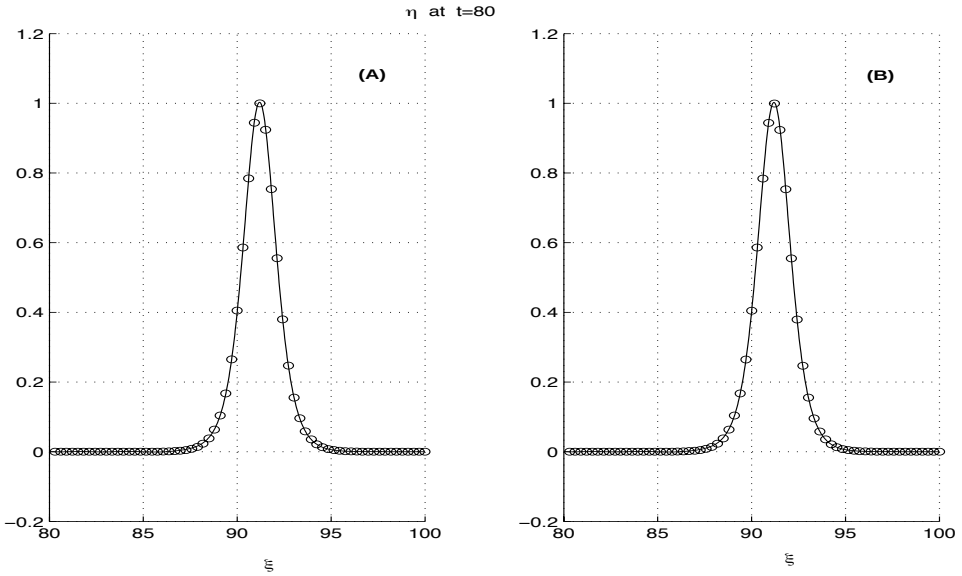

FIG. 4.1. *Propagation of the solitary wave for model (3.3)-(3.4) with* $\alpha = \beta = 0.03$. *Convention: solid line indicates the numerical solution and the dots profile (4.7).* **(A)** *Boussinesq model with depth parameter* $Z_0 = \sqrt{1/5}$. **(B)** *with* $Z_0 = 0.469$.

4.2. Numerical scheme for the linear potential theory equations. Consider the linearization of equations (2.19)-(2.22)

$$\beta\phi_{\xi\xi} + \phi_{\zeta\zeta} = 0, \quad \text{for} \quad 0 < \zeta < 1, \tag{4.9}$$

$$\eta_t - \frac{1}{\beta M(\xi)}\phi_\zeta = 0, \quad \text{at} \quad \zeta = 1, \tag{4.10}$$

$$\eta + \phi_t = 0, \quad \text{at} \quad \zeta = 1, \tag{4.11}$$

$$\phi_\zeta = 0, \quad \text{at} \quad \zeta = 0, \tag{4.12}$$

subject to the initial conditions

$$\phi(\xi, 1, 0) = \phi_0(\xi), \quad \eta(\xi, 0) = \eta_0(\xi).$$

At the time stage $(n+1)\Delta t$ we discretize the equations at the free surface $\zeta = 1$

by

$$\frac{\eta^{n+1}-\eta^n}{\Delta t}-\frac{\phi_\zeta^{n+1}+\phi_\zeta^n}{2\beta M(\xi)}=O(\Delta t^2), \tag{4.13}$$

$$\frac{\phi^{n+1}-\phi^n}{\Delta t}+\eta^n+\frac{\Delta t}{2\beta M(\xi)}\phi_\zeta^n=O(\Delta t^2). \tag{4.14}$$

This scheme in time is basically the same as used in [25, 26, 27]. It is perfectly suited for the Dirichlet-to-Neumann (DtN) formulation presented by Artiles and Nachbin [1, 2] as we shall describe. Having an expression for the DtN operator enables writing a highly efficient and highly accurate numerical scheme, without any truncation errors in space. By the construction of the DtN operator presented in [1, 2], the normal derivative at the free surface can be computed through

$$\phi_\zeta(\xi,1,t)=\frac{1}{2\pi}\int_{-\infty}^{\infty}k\sqrt{\beta}tanh(\sqrt{\beta}k)\hat{\phi}(k,1,t)e^{ik\xi}dk. \tag{4.15}$$

This expression is exact and automatically satisfies Laplace's equation (4.9). Moreover it can be easily evaluated through the FFT algorithm. Here the hat denotes the Fourier transform with respect to the spatial coordinate ξ. In conclusion at any fixed time t equation (4.15) transforms Dirichlet data ($\phi(\xi,1,t)$) into the corresponding Neumann data along the (linear) free surface of the fluid ($\zeta=1$). A nonlinear DtN operator was also described in [1, 2]. Its numerical implementation is currently under investigation.

5. Numerical experiments. In this section, we will compare model (3.3)-(3.4) with $Z_0=0.469$ (the optimal value of the depth parameter, c.f. section 3.1), the terrain-following Boussinesq system (2.25)-(2.26), both with the original linear ($\alpha=0$) potential theory equations in curvilinear coordinates (2.19)-(2.22). This will be performed through a suite of numerical experiments performed by using the Boussinesq solvers described in section 4. We only consider the linear regime for the potential theory equations in order to fully focus on the dispersion issues discussed earlier. Simulations with the full nonlinear potential equations will appear in a future work.

Given a pair (f,g) of initial data for the potential theory equations (2.19)-(2.22) we will explain how to compute the corresponding initial data for the Boussinesq systems (3.3)-(3.4) and (2.25)-(2.26). This is the main difficulty in comparing the solutions of these models because the dependent variables are not the same. We proceed as follows.

Let Ω denote the rectangle bounded by $\zeta=0$, $\zeta=1$, $\xi=0$ and $\xi=L$, $L>0$. Let us give the free surface data (ϕ,η) for equations (2.19)-(2.22). Then we compute the corresponding initial potential profile $\phi(\xi,Z_0,0)$ (at the depth $\zeta=Z_0$ and time $t=0$) by the contour integral

$$\phi(\xi,\zeta=Z_0,0)=\frac{1}{2\pi\sqrt{\beta}}\oint_{\partial\Omega}\left(\phi(Q,0)G_{\tilde{n}}(P,Q)-\phi_{\tilde{n}}(Q,0)G(P,Q)\right)dQ. \tag{5.1}$$

We use the notation: $P=(\xi,Z_0)$, $Q=(\tilde{\xi},\tilde{\zeta})$, $\phi_{\tilde{n}}=(\beta\phi_\xi,\phi_\zeta).\vec{n}$ ($\vec{n}$ denotes the outer normal vector at the boundary $\partial\Omega$), with the Green's function

$$G(\xi,\zeta,\tilde{\xi},\tilde{\zeta})=\frac{1}{2}ln((\xi-\tilde{\xi}^2+\beta(\zeta-\tilde{\zeta})^2)+\frac{1}{2}ln((\xi-\tilde{\xi}^2+\beta(\zeta+\tilde{\zeta})^2). \tag{5.2}$$

We remark that equation (5.1) is a consequence of Green's third identity. Details can be found in [25, 26, 27]. Note also that kernel G is such that $G_{\tilde{n}} = 0$ at the channel bottom $\zeta = 0$ and $\Delta_{(\xi,\zeta)} G(P,Q) = \delta_P(Q)$, where $\delta_P(Q)$ represents the Dirac delta function. Now, since $\phi_\zeta = 0$ at the bottom $\zeta = 0$, and assuming that $\phi, \phi_{\tilde{n}}$ tend to zero when $|\xi| \to \infty$, we have that when $L \to \infty$, the contour integral in (5.1) needs only to be evaluated along the free surface $\zeta = 1$. Namely,

$$\phi(\xi, \zeta = Z_0, 0) = \frac{1}{2\pi\sqrt{\beta}} \int_{-\infty}^{\infty} \left(\phi(\tilde{Q}, 0) G_{\tilde{n}}(P, \tilde{Q}) - \phi_{\tilde{n}}(\tilde{Q}, 0) G(P, \tilde{Q}) \right) d\tilde{\xi}, \tag{5.3}$$

where $\tilde{Q} = (\tilde{\xi}, 1)$. This reduces the number of grid points along the contour by at least 50 percent. The topography *does not need to be discretized* and its effect is built into the (smooth) free surface coefficient $M(\xi)$. Once the initial velocity potential is computed by the numerical evaluation of the integral, the initial value for the velocity of the Boussinesq model (3.3)-(3.4) is calculated as $u(\xi, 0) = u_0(\xi) = \phi_\xi(\xi, Z_0, 0)$. We remark that the wave elevation at $t = 0$, $\eta(\xi, 0) = \eta_0(\xi)$ coincides in both models.

5.1. Constant depth experiments. The goal of our first experiment is to give evidence of some results from the dispersion analysis performed for the Boussinesq models considered, in respect to the potential theory equations (2.19)-(2.22). This is done in the case where the depth is constant. We set $\beta = 0.2$ and $\alpha = 0.001$, i.e. we have nontrivial dispersion and the regime is effectively linear.

To keep our focus on the full dispersion relation we solve the linear potential theory equations (4.9)-(4.12) on the computational domain $[0, 20\pi]$, with $\Delta t = 0.0063$ and 8192 FFT points in the spatial mesh (where $\Delta\xi = 0.00767$). The boundary conditions are periodic but no activity will be observed at the extremes of the interval $[0, 20\pi]$. The initial conditions are

$$\Phi(\xi, 1, 0) = \Phi_0(\xi) = \sqrt{\frac{10}{\pi}} e^{-5(\xi-20)^2},$$
$$\eta(\xi, 0) = \eta_0(\xi) = -10\sqrt{\frac{10}{\pi}} (\xi - 20) e^{-5(\xi-20)^2}.$$

These conditions produce right and left going waves when $\beta \neq 0$. Nevertheless the left going wave tends to zero as $\beta \downarrow 0$ [26, 35]. Remark that once the solution to the equations (4.9)-(4.12) are known, then the initial fluid velocity for the Boussinesq models is computed through the equation (5.3) as explained above. The parameters for solving the system (2.25)-(2.26) are $\Delta t = 0.0063$, $\Delta\xi = 0.0077$. In figure 5.1 we superimpose the solutions of models (4.9)-(4.12) and (2.25)-(2.26) at time $t = 25$. We observe that they coincide with good accuracy in the interval [36,50] corresponding to the wavefront, namely of low wavenumber content [35]. As expected, the signals in the interval [5,35] differ due to the truncation errors introduced by neglecting the terms of order $O(\beta^2)$ in the Boussinesq model (3.3)-(3.4).

In figure 5.2 the solution of system (3.3)-(3.4) with the optimal value of the depth parameter $Z_0 = 0.469$ (computed as explained in section 3.1) is compared with the original equations (4.9)- (4.12). The numerical parameters are the same as before. In contrast to the previous experiment, the solutions match with good accuracy in the whole interval [5,50]. The Boussinesq system (3.3)-(3.4) captures well the dispersive details of the oscillatory coda of the propagating signal. In figure 5.1 the mismatch along the coda is due to the large phase errors as depicted in figure 3.1.

These experiments are in agreement with the linear dispersion analysis performed in section 3.1 and the theory presented in appendix A.

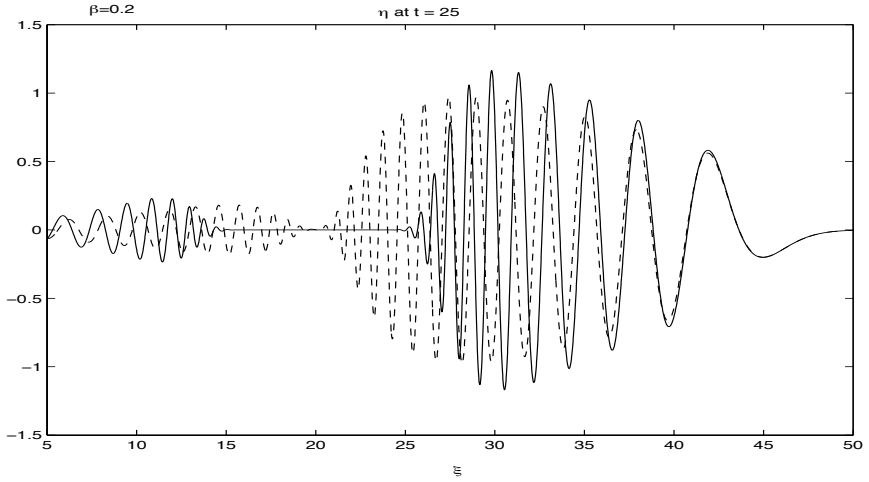

FIG. 5.1. *A rightgoing wavetrain to the right and a small leftgoing wavetrain to the left. Dashed line: Numerical solution of the terrain-following system (2.25)-(2.26). Solid line: Numerical solution of the equations (4.9)-(4.12). Model parameters:* $\alpha = 0$, $\beta = 0.2$.

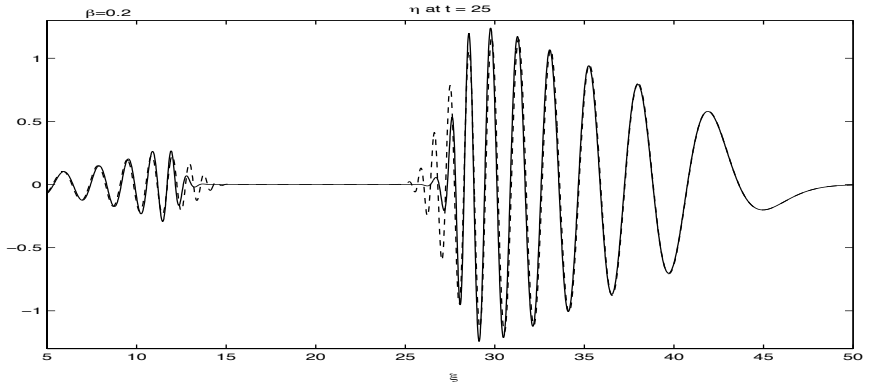

FIG. 5.2. *Dashed line: Numerical solution of system (3.3)-(3.4) with* $Z_0 = 0.469$. *Solid line: Numerical solution of the equations (2.19)-(2.22). Model parameters:* $\alpha = 0$, $\beta = 0.2$.

5.2. Highly variable topography. We have tested the different models over a flat bottom and now we are in a position to perform experiments in the presence of an irregular bottom. We will consider two levels of dispersion in the models. The variable coefficient $M(\xi)$ is taken to be of the form

$$M(\xi) = 1 + \delta n(\xi/\gamma),$$

where $n(\xi/\gamma)$ is a mean-zero piecewise linear function constructed by using a random number generator in the interval [-1,1] and δ measures the amplitude of the fluctuations. The constant γ measures the relative scale of variation of the bottom irregularities. We consider γ to be small. This type of synthesized function has been

employed by several researchers in order to validate pulse shaping theory in random media [4, 8, 12, 7]. Maintaining our focus on the linear regime we will examine how the reduced Boussinesq model captures the fine features of the topography in contrast with the potential theory model.

We start by fixing a very small dispersion parameter value $\beta = 0.002$. In figure 5.3 we compare the solution (i.e. a multiply scattered segment of the wave) of equations (4.9)-(4.12) with the solution of the model (2.25)-(2.26). The numerical parameters for equations (4.9)-(4.12) are $\Delta t = 0.01$, 2^{12} FFT points in space where the computational domain is [0,150]. The numerical parameters for solving system (2.25)-(2.26) are $\Delta\xi = 0.024$, $\Delta t = 0.0125$ and the computational domain is [0,120]. The irregularities of the coefficient $M(\xi)$ covers the interval [67,107] and the fluctuations are such that $\delta = 0.5$ and $\ell = 0.1$. The initial conditions for equations (2.19)-(2.22) are

$$\Phi(\xi, 1, 0) = \Phi_0(\xi) = e^{-20(\xi-60)^2},$$
$$\eta(\xi, 0) = \eta_0(\xi) = -40(\xi - 60)e^{-20(\xi-60)^2}.$$

Here we are considering a shorter pulse (hence having a broader band in wavenumber space) to show the broad range of applicability of the numerical method and also of the dispersion analysis presented. The corresponding initial velocity at $Z_0 = \sqrt{1/3}$ for the system (2.25)-(2.26) is calculated from equation (5.3). Observe in figure 5.3 that the solutions of the original potential theory equations and the approximated Boussinesq model agree well. We are graphing the region where we measured the maximum value of the error. Over the rest of the computational domain the solutions agree even better.

In figure 5.4 we compare the solution of equations (4.9)-(4.12) to the solution of the model (3.3)-(3.4) for the optimal value of the depth parameter $Z_0 = 0.469$. The numerical parameters for the model equations are the same as in the previous experiment. The corresponding solutions of the two models agree with even better accuracy.

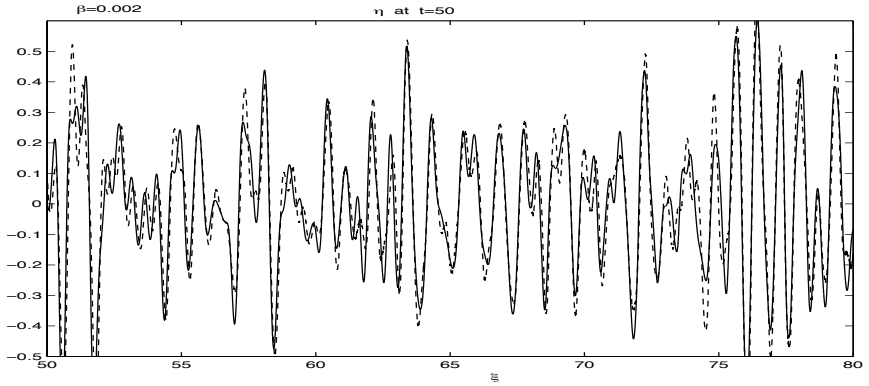

FIG. 5.3. *Dashed line: Numerical solution of the terrain-following system (2.25)-(2.26). Model parameters:* $\alpha = 0.001$, $\beta = 0.002$. *Solid line: Numerical solution of the equations (4.9)-(4.12). Model parameters:* $\alpha = 0$, $\beta = 0.002$.

An additional experiment (figure 5.5) is performed for $Z_o = \sqrt{2/3}$, keeping $\alpha = 0.001$, $\beta = 0.002$. This is the best value for the depth parameter in order to prove theorems regarding solution properties in function space [6, 32]. Nevertheless the comparison with potential theory is not as good as for $Z_0 = 0.469$.

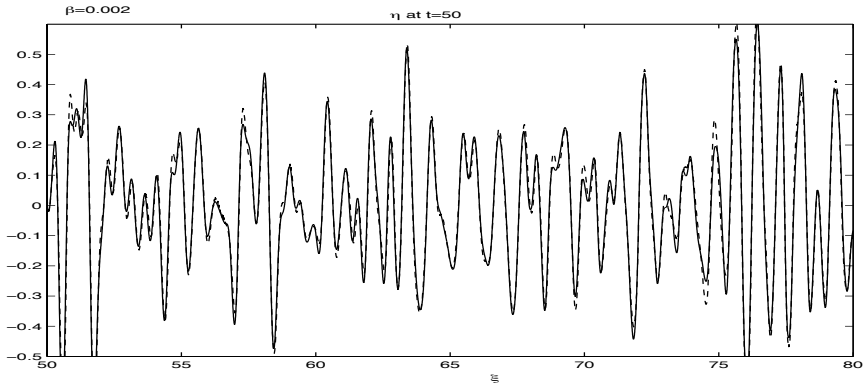

FIG. 5.4. *Dashed line: Numerical solution of the Boussinesq system (3.3)-(3.4). Model parameters:* $\alpha = 0.001$, $\beta = 0.002$, $Z_0 = 0.469$. *Solid line: Numerical solution of the equations (4.9)-(4.12). Model parameters:* $\alpha = 0$, $\beta = 0.002$.

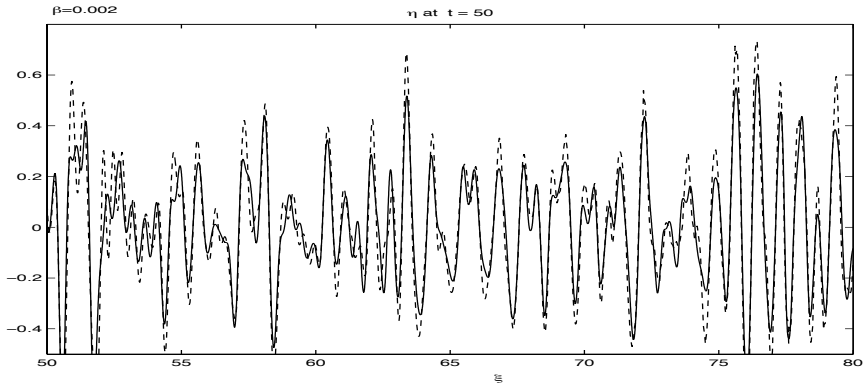

FIG. 5.5. *Dashed line: Numerical solution of the system (3.8)-(3.9). Model parameters:* $\alpha = 0.001$, $\beta = 0.002$, $Z_o = \sqrt{2/3}$. *Solid line: Numerical solution of the equations (4.9)-(4.12). Model parameters:* $\alpha = 0$, $\beta = 0.002$.

Now we increase the dispersion parameter to $\beta = 0.05$. In figure 5.6 we contrast the solution for equations (4.9)-(4.12) with the solution of model (2.25)-(2.26). We use the same numerical parameters as in the preceding experiments. We take a different realization of the metric coefficient $M(\xi)$ in this set of experiments to show that the results are generic. In this case, the error introduced when the dispersive terms are truncated in the Boussinesq model (3.3)-(3.4) (with $Z_0 = \sqrt{1/3}$) is appreciable.

To contrast with the preceding experiment, in figure 5.7 we compare the solutions for equations (4.9)-(4.12) with those for system (3.3)-(3.4) with $Z_0 = 0.469$. As explained in section 3.1, for this particular value of the depth parameter Z_0, the smaller relative error in phase velocity for the models considered makes the difference. Now, the solutions agree well inside the region [67,107] where the fluctuations of the topography are located. This experiment provides strong evidence that the new Boussinesq formulation (3.3)-(3.4) (with $Z_0 = 0.469$) enables an improved prediction for the pulse reflection with respect to the terrain-following system (2.25)-(2.26). This behaviour was observed systematically in several numerical experiments performed for different levels of the dispersion parameter β.

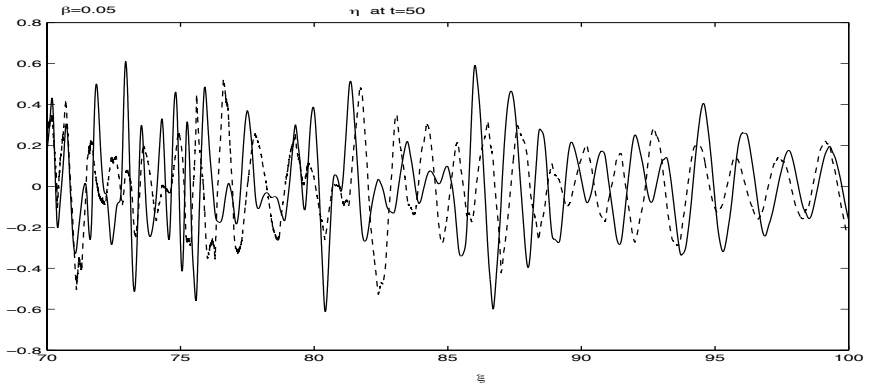

FIG. 5.6. *Dashed line: Numerical solution of the terrain-following system (2.25)-(2.26). Model parameters:* $\alpha = 0.001$, $\beta = 0.05$. *Model parameters:* $\alpha = 0.001$, $\beta = 0.05$. *Solid line: Numerical solution of the equations (4.9)-(4.12). Model parameters:* $\alpha = 0$, $\beta = 0.05$.

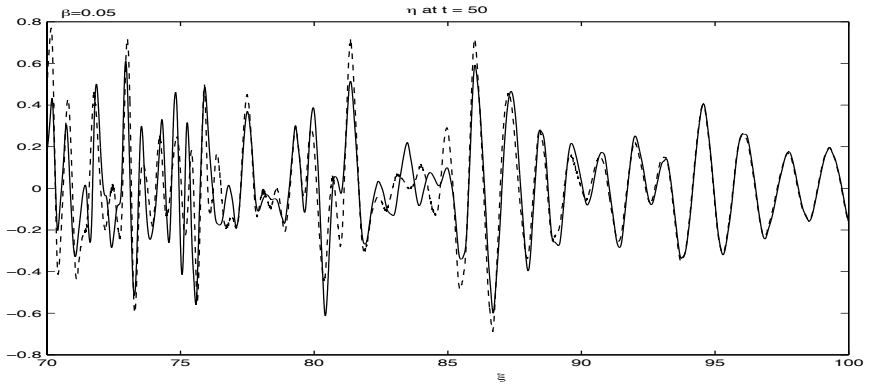

FIG. 5.7. *Dashed line: Numerical solution of system (3.3)-(3.4) with* $Z_0 = 0.469$. *Model parameters:* $\alpha = 0.001$, $\beta = 0.05$. *Solid line: Numerical solution of the equations (4.9)-(4.12) . Model parameters:* $\alpha = 0$, $\beta = 0.05$.

Finally consider the (optimal L^2 norm) value $Z_o = \sqrt{1/5} = 0.447$. This value is no that different from 0.469. Nevertheless some differences in the highly fluctuating part of the scattered signal can be noticed (c.f. figure 5.8).

6. Waveform inversion by time reversal refocusing. Time-reversal experiments can be performed for the transmitted (TRT) or for the reflected (TRR) signal as schematically indicated in figure 6.1. The transmitted (or reflected signal) is recorded at the corresponding extreme of the inhomogeneous medium. The data is time reversed and sent back into the same medium through the exact same model. By *time reversion* it is meant that information recorded last is sent out first. In other words the recorded signal is used as a new initial data, for *the same system* of partial differential equations, but it is propagated backwards into the (same) inhomogeneous medium, as indicated in figure 6.1. Much mathematical and experimental work has been done showing that this process leads to the recompression of the noisy signal into the original pulse shape. In particular laboratory experiments were done for acoustic waves [11]. For mathematical details please consult [24, 13] and the references

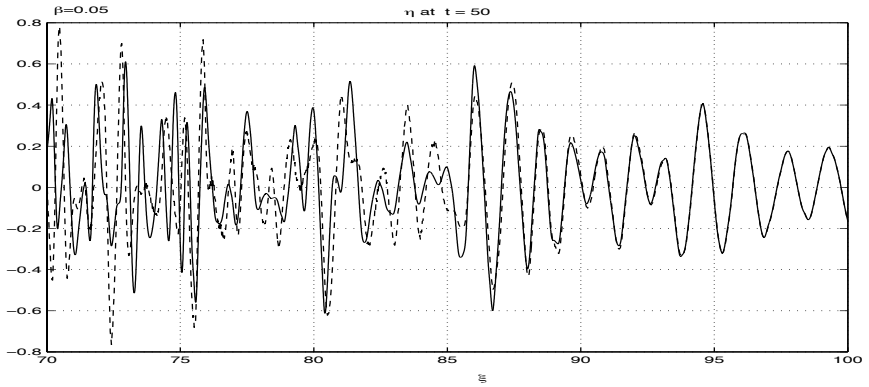

FIG. 5.8. *Dashed line: Numerical solution of the system (3.3)-(3.4) with* $Z_0 = \sqrt{1/5}$. *Model parameters:* $\alpha = 0.001$, $\beta = 0.05$. *Solid line: Numerical solution of the equations (2.19)-(2.22). Model parameters:* $\alpha = 0$, $\beta = 0.05$.

therein, which include several leading work by Papanicolaou and collaborators. One of our recent goals has been to study the time-reversal refocusing for solitary waves. In previous work, we have mathematically analysed the effect of dispersion [13] and the effect of nonlinearity [14] separately. Nevertheless to the present date there is no theory for the time-reversed refocusing of solitary waves or solitons of any kind. Numerical simulations with solitary waves have been presented in [24, 15] and are further explored in the present paper through the improved Boussinesq model. We hope that this experimental study will eventually lead to new mathematical theory.

Regarding applications in water waves, the problem of waveform inversion has been studied by adjoint methods as in Pires and Miranda [31] and the references within. Their goal is to characterize the initial sea surface displacement due to tsunamigenic earthquakes. In other words one would like to recover (numerically) relevant details of a tsunami source from tidal gauge observations. In our case, instead of performing the backward numerical integration for the corresponding adjoint equations, we use the (same) forward numerical model but with the time-reversed data as explained above. Waveform inversion is obtained through the time-reversed refocusing effect. The advantage regarding time-reversal methods is for nonlinear problems. For adjoint methods there are technical difficulties involved with nonlinearity as reported by Pires and Miranda [31].

The purpose of this section is to revisit the refocusing phenomenon, now in the case of the system (3.3)-(3.4) with the optimal depth $Z_0 = 0.469$. We also present time reversal simulations with the potential theory equation. We note that this has never been done before. The goal is to observe the improved waveform inversion procedure in comparison with earlier experiments. Namely, up to now, all the dispersive time reversal refocusing experiments were performed for the depth-averaged Boussinesq system, which amounts to $Z_0 = \sqrt{1/3}$ [24, 13, 15]. In addition, we will further explore the refocusing of solitary waves, for different values of the amplitude of the topography fluctuations and of the correlation length of the irregularities.

Throughout this section, the numerical parameters for equations (4.9)-(4.12) are $\Delta t = 0.01$, 2^{12} FFT points in space and the computational domain is [0,150]. The numerical parameters for systems (2.25)-(2.26) and (3.3)-(3.4) are $\Delta\xi = 0.024$, $\Delta t = 0.0125$ and the computational domain is [0,120]. The irregularities of the coefficient

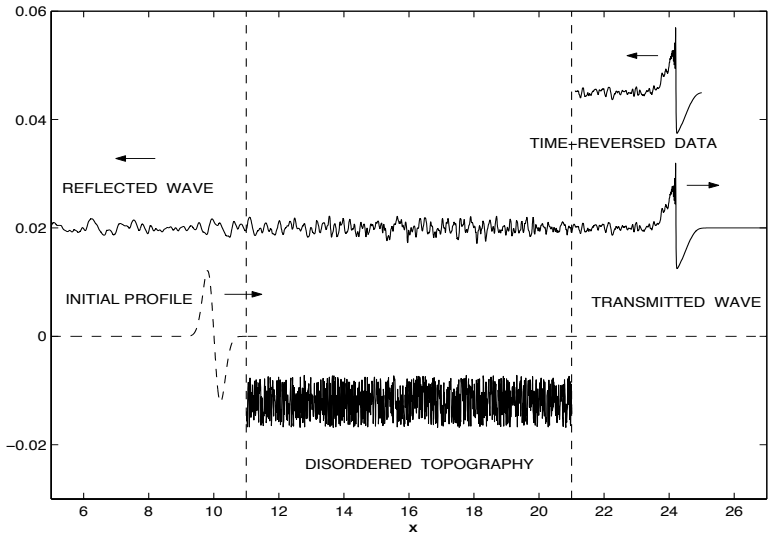

FIG. 6.1. *Schematic figure for time reversal simulations.*

$M(\xi)$ are located in the interval [67,107] and again $\delta = 0.5$ and $\ell = 0.1$.

6.1. TRR refocusing of Gaussian pulses. The first experiment uses $\beta = 0.002$ and $\alpha = 0.001$ indicating a weakly dispersive, effectively linear regime. The pulses are the same as before, namely

$$\Phi(\xi, 1, 0) = \Phi_0(\xi) = e^{-20(\xi-60)^2},$$
$$\eta(\xi, 0) = \eta_0(\xi) = -40(\xi - 60)e^{-20(\xi-60)^2}.$$

Note that for a time-reversal in reflection (TRR) experiment we only record the reflected signal, recorded to the left of the topography (c.f. figure 6.1). Hence this fluctuating signal has no indication whatsoever of the original pulse shape, say as opposed to the transmitted wave. These fluctuating signals (for η and u) are sent back into the inhomogeneous medium and by the refocusing phenomenon they recompress into a (reduced) copy of their initial pulse shapes.

We emphasize that the pulse shape is exactly the same [13]: in the present experiment it is the derivative of a Gaussian as shown in figure 6.2. In figure 6.2 the refocused pulse obtained from model (4.9)-(4.12) is superimposed to the one obtained from system (2.25)-(2.26). Observe that the refocused pulses obtained from both models agree with very good accuracy and that they are derivatives of a Gaussian (as expected) of a reduced amplitude. The reduction in amplitude is intuitive since there is a nontrivial amount of energy being transmitted to the other side of the topography. Hence TRR recompresses only a fraction of the initial energy [15].

In an analogous way, in figure 6.3 we observe that the refocused pulse obtained with the model (2.19)-(2.22) coincides to that of system (3.3)-(3.4) with $Z_0 = 0.469$. This is expected since the dispersion level is low ($\beta = 0.002$).

In the second experiment we increase the level of dispersion by a factor of 25 ($\beta = 0.05$). Again we adopt a different realization of the coefficient $M(\xi)$ in this experiment to show that the results are generic. In figure 6.4 we compare the refocused pulse obtained with model (4.9)-(4.12) with that of system (2.25)-(2.26). Now observe

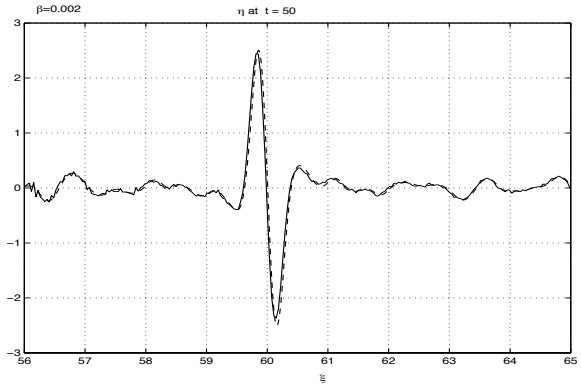

FIG. 6.2. *In solid line: TRR refocusing for system (4.9)-(4.12). Model parameters:* $\alpha = 0$, $\beta = 0.002$. *In dashed line: TRR refocusing for system (2.25)-(2.26). Model parameters:* $\alpha = 0.001$, $\beta = 0.002$.

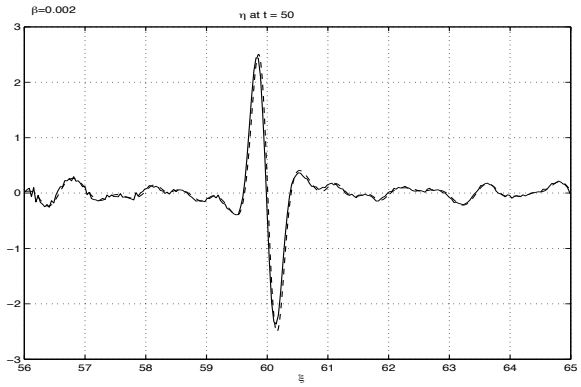

FIG. 6.3. *In solid line: TRR refocusing for system (4.9)-(4.12). Model parameters:* $\alpha = 0$, $\beta = 0.002$. *In dashed line: TRR refocusing for system (3.3)-(3.4). Model parameters:* $\alpha = 0.001$, $\beta = 0.002$, $Z_0 = 0.469$.

that the corresponding solutions are quit different. In particular, the relative error in the pulses' peaks is roughly 40 percent.

In figure 6.5 we compare the refocused pulse obtained with the model (4.9)-(4.12) to that of system (3.3)-(3.4) with $Z_0 = 0.469$. In contrast with the previous experiment, observe that the Boussinesq prediction agrees very well at the pulses' peak and even along the fluctuating part of the signal. The TRR refocusing phenomenon highlights, in a quite dramatic fashion, the improvements of the Boussinesq system: waveform inversion with another Boussinesq system (as the one we used in [13, 15]) can underestimate, say, the initial amplitude of a tsunami [31]. It is important to say that the theory and computations in [13, 15] were correct but, as shown in this paper, done with a restrictive model. The TRR refocusing phenomenon also works well for $Z_0 = \sqrt{1/5}$.

6.2. TRT refocusing of Gaussian pulses. We now perform TRT as schematically indicated in figure 6.1. In this case usually we observe a leading wavefront followed by a fluctuating coda. The fluctuating coda consists of a dispersive tail as well as of a disordered component, generated due to the forward scattering. This can be

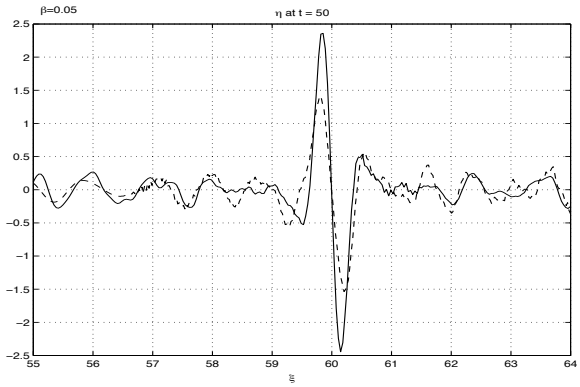

FIG. 6.4. *In solid line: TRR refocusing for system (2.19)-(2.22). Model parameters:* $\alpha = 0$, $\beta = 0.05$. *In dashed line: TRR refocusing for system (2.25)-(2.26). Model parameters:* $\alpha = 0.001$, $\beta = 0.05$.

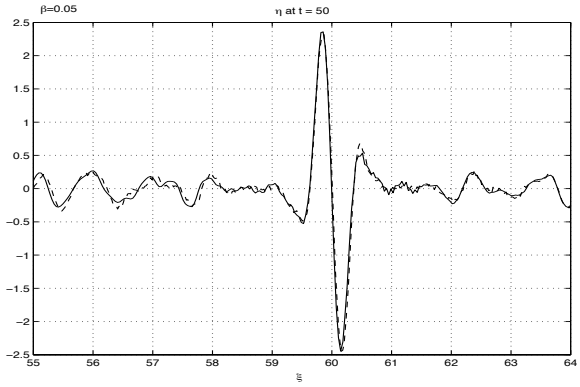

FIG. 6.5. *In solid line: TRR refocusing for system (2.19)-(2.22). Model parameters:* $\alpha = 0$, $\beta = 0.05$. *In dashed line: TRR refocusing for system (3.3)-(3.4). Model parameters:* $\alpha = 0.001$, $\beta = 0.05$, $Z_0 = 0.469$.

clearly seen in figure 6.6 where the smooth (Airy-like) wavefront is about to leave the region where the topography is located. The wavefront, the dispersive tail and the disordered coda are all recorded to the right of the topography. We set $\beta = 0.05$. The numerical parameters for the potential theory equations (4.9)-(4.12) are $\Delta t = 0.01$, 2^{13} FFT points in space and the computational domain is [0,290]. The numerical parameters for systems (2.25)-(2.26) and (3.3)-(3.4) are $\Delta t = 0.013$, $\Delta\xi = 0.029$ and the computational domain is [0,290]. The initial conditions for equations (2.19)-(2.22) are

$$\Phi(\xi, 1, 0) = \Phi_0(\xi) = e^{-20(\xi-150)^2},$$
$$\eta(\xi, 0) = \eta_0(\xi) = -40(\xi - 150)e^{-20(\xi-150)^2}.$$

Observe that the initial pulses are located at the position $\xi = 150$. We recall that the corresponding initial velocity at the level Z_0 for systems (2.25)-(2.26) and (3.3)-(3.4) is calculated from equation (5.3).

In figure 6.7 we compare the refocused pulse obtained with the model (4.9)-(4.12) to the one obtained with system (2.25)-(2.26). In figure 6.8 we compare the refocused

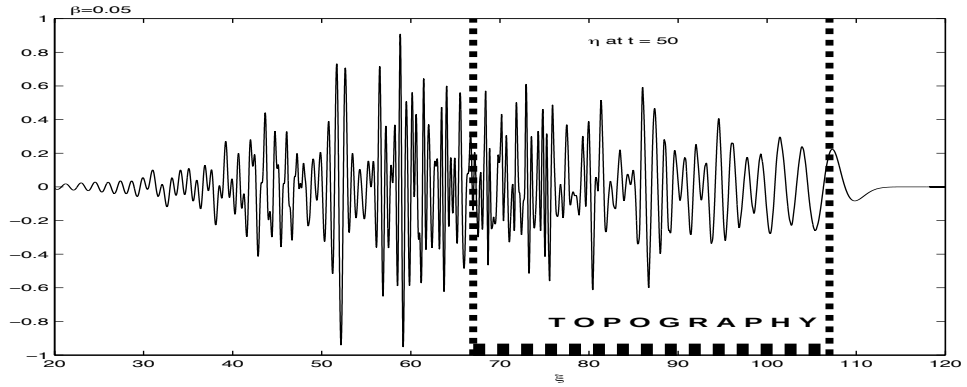

FIG. 6.6. *An example of the entire wave profile, computed from the potential theory equations (4.9)-(4.12).*

pulse obtained with potential theory to that of system (3.3)-(3.4) with $Z_0 = 0.469$. One can see some improvement. The improvement for TRT is not so dramatic as for TRT. The reason is that for TRT the bulk of the energy is still contained in the leading wavefront. In other words most of energy resides on low wavenumbers and therefore the dispersive effects are less noticeable.

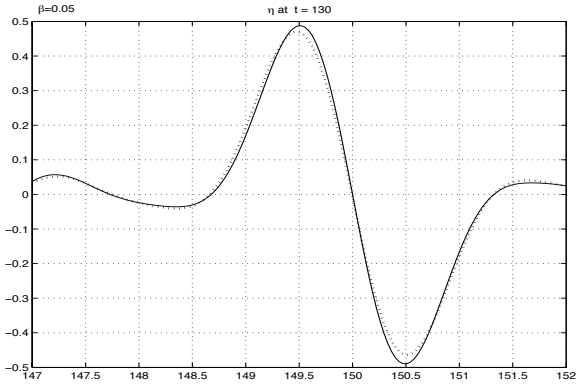

FIG. 6.7. *In solid line: TRT refocusing for system (4.9)-(4.12). Model parameters:* $\alpha = 0$, $\beta = 0.05$. *In dashed line: TRT refocusing for system (2.25)-(2.26). Model parameters:* $\alpha = 0.001$, $\beta = 0.05$.

6.3. TRR refocusing for solitary waves. In this section we analyze the refocusing property for solitary waves of system (3.3)-(3.4). Recall that equation (4.7) furnishes a solitary wave solution for a second order Boussinesq-type equation formally equivalent to equations (3.3)-(3.4). The length scale for the irregularities of the coefficient $M(\xi)$ is $\ell = 0.6$ because the effective support of the solitary wave (4.7) is $\ell_p = 6$. Thus, we preserve the ratio $\gamma = \ell/\ell_p = 1/10$. The initial solitary wave is located at the position $\xi = -5$. The amplitude of the irregularities is $\delta = 0.5$. The irregularities of the metric coefficient $M(\xi)$ are in the interval [5,305]. In this set of experiments, the numerical parameters are $\Delta t = 0.0375$, $\Delta\xi = 0.04266$, and the computational domain is [-320,320].

In the first experiment we adopt $\alpha = \beta = 0.01$. Just as for the Gaussian pulse we

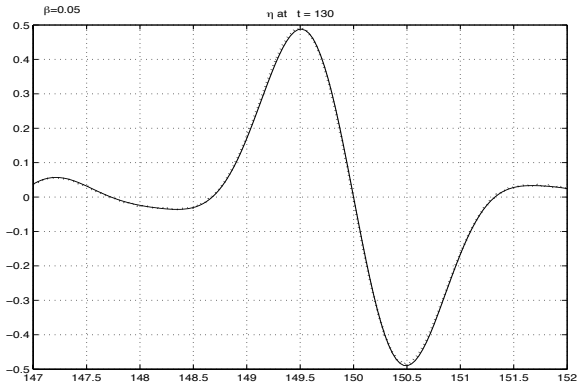

FIG. 6.8. *In solid line: TRT refocusing for system (4.9)-(4.12). Model parameters:* $\alpha = 0$, $\beta = 0.05$. *In dashed line: TRT refocusing for system (3.3)-(3.4). Model parameters:* $\alpha = 0.001$, $\beta = 0.05$, $Z_0 = 0.469$.

record the reflected signal to the left of the topography. We time reverse the data and use it as the initial condition for the exact same problem. This time reversed fluctuating data travels towards the rough region and, after interacting with the topography, it recompresses into the smooth pulse shown at the center of figure 6.9. There is no theory to tell us what kind of pulse we are seeing after refocusing. It is not clear that we have a reduced copy of the solitary wave.

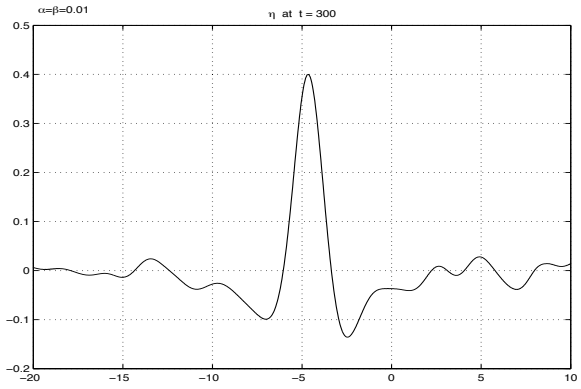

FIG. 6.9. *TRR refocusing of the solitary wave (4.7) of the system (3.3)-(3.4) with* $Z_0 = 0.469$. *Numerical parameters:* $\alpha = \beta = 0.01$.

In the second experiment we repeat the previous experiment but now we set $\alpha = \beta = 0.03$. This experiment is more dispersive and nonlinear than the previous one. The refocused pulse is presented in figure 6.10 and very much resembles the previous case. The phenomenon is robust regarding the dispersion and nonlinearity levels.

Now we vary some other parameters related to the propagation medium (i.e. topography) rather than the wave. We repeat the previous experiment (keeping $Z_o = 0.469$) but now with a smaller fluctuation level: $\delta = 0.25$. This implies in a weaker reflected signal. A plausible question is to whether the weak reflected signal will contain enough energy to produce a well defined refocused pulse. The answer is

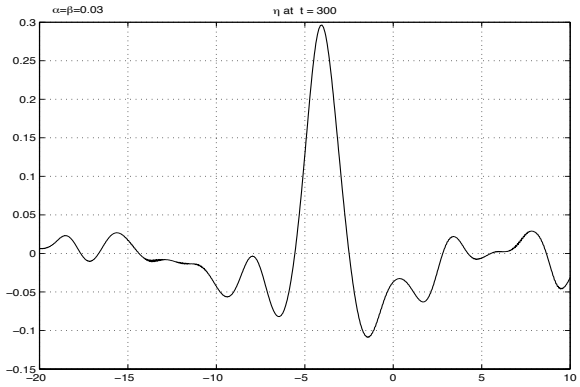

FIG. 6.10. *TRR refocusing of the solitary wave (4.7) of the system (3.3)-(3.4) with* $Z_0 = 0.469$. *Numerical parameters:* $\alpha = \beta = 0.03$.

clearly seen in figure 6.11 where we have a clean refocused pulse, but of a smaller amplitude (since it contains less energy).

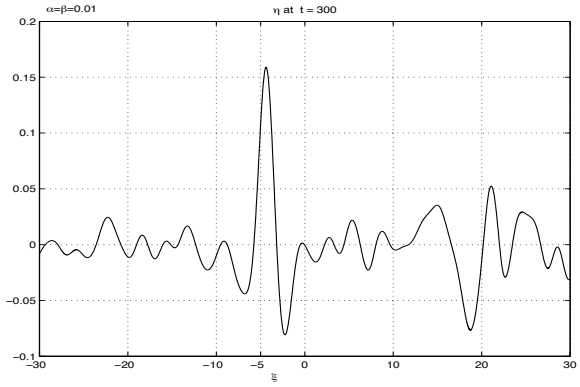

FIG. 6.11. *TRR refocusing of the solitary wave (4.7) of system (3.3)-(3.4) with* $Z_o = 0.469$. *Model's parameters:* $\alpha = \beta = 0.01$, *fluctuation level* $\delta = 0.25$.

Next we change the correlation length adopted to be $\ell = 0.3$, which is half of that in the previous experiments. Now the topography is even more rapidly varying and long waves can not feel it in detail. The amplitude of fluctuations is back to $\delta = 0.5$. Observe that the amplitude of the refocused pulse is approximately 30 % of the initial solitary wave (4.7). Compare with figure 6.9 where ($\ell = 0.6$, $\delta = 0.5$) and the refocused pulse amplitude was at the 40 % level. As mentioned above, here the topography is on an even finner scale, so that the solitary wave feels less the details and therefore sheds less reflection.

The important fact about all these experiments is that the refocusing phenomenon is very robust for solitary waves.

7. Conclusion. We have used ideas from Nwogu [29] to improve Boussinesq models in the presence of highly-variable (multiscale) depth profiles. We presented a linear dispersion analysis and numerically validated the corresponding results. Validation was done by comparing them with the corresponding linear potential theory.

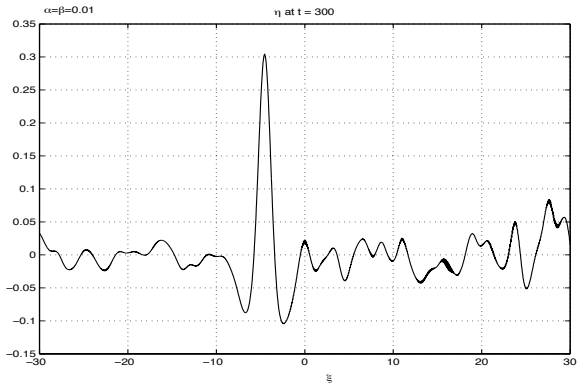

FIG. 6.12. *TRR refocusing of the solitary wave (4.7) of system (3.3)-(3.4) with* $Z_o = 0.469$. *Model's parameters:* $\alpha = \beta = 0.01$.

We showed the excellent performance of the improved Boussinesq system in the presence of highly disordered topographies. Discrepancies observed among the different Boussinesq models became even more important in the waveform inversion problem. In this problem we adopted the time reversal technique for recompressing a long fluctuating signal, representing a highly scattered wave that has propagated for very long distances. The scattered signal refocused into a smooth profile. In particular we showed that this phenomenon is very robust even for solitary waves. The case for solitary waves can only be done numerically because there is no theory to predict the refocused pulse shape.

Appendix A. Analytic comparison of the linearized models. Bona and Chen [5] derived L^2 estimates for the difference between linear solutions of the KdV equation and of another KdV-type equation. In this appendix we extend their analysis and compare linear solutions of the Boussinesq equations (3.3)-(3.4) with those for the potential theory equations (2.19)-(2.22). Hence we restrict ourselves to the linear case (i.e. $\alpha = 0$) and constant depth ($M \equiv 1$). Further we recall that the dispersion parameter β is small in this analysis.

In first place, the linearized Boussinesq system reads

$$\eta_t + u_\xi + \frac{\beta}{2}(Z_0^2 - 1/3)u_{\xi\xi\xi} = 0, \tag{A.1}$$

$$u_t + \eta_\xi + \frac{\beta}{2}(Z_0^2 - 1)u_{\xi\xi t} = 0, \tag{A.2}$$

$$u(\xi, 0) = f(\xi), \quad \eta(\xi, 0) = \eta_0(\xi), \tag{A.3}$$

and the linear potential equations are

$$\beta\phi_{\xi\xi} + \phi_{\zeta\zeta} = 0, \quad \text{for } 0 < \zeta < 1, \tag{A.4}$$

$$\begin{aligned} \eta_t - \frac{1}{\beta}\phi_\zeta &= 0, \quad \text{at } \zeta = 1, \\ \eta + \phi_t &= 0, \quad \text{at } \zeta = 1, \\ \phi_\zeta &= 0, \quad \text{at } \zeta = 0, \\ \phi(\xi, 1, 0) = \phi_0(\xi), \quad \eta(\xi, 0) &= \eta_0(\xi). \end{aligned} \tag{A.5}$$

In order to eliminate the parameter β in the equations above, we introduce the change of variables

$$\phi(\xi,\zeta,t) = \beta^{-1/2}\Phi(\beta^{-1/2}\xi,\zeta,\beta^{-1/2}t),$$
$$\eta(\xi,t) = \beta^{-1}N(\beta^{-1/2}\xi,\beta^{-1/2}t),$$
$$u(\xi,t) = \beta^{-1}U(\beta^{-1/2}\xi,\beta^{-1/2}t).$$

Therefore, the new initial data in the variables U, N, Φ are $N(\xi,0) = N_0(\xi) = \beta\eta_0(\beta^{1/2}\xi)$, $U(\xi,0) = F(\xi) = \beta f(\beta^{1/2}\xi)$ and $\Phi(\xi,1,0) = \Phi_0(\xi) = \beta^{1/2}\phi_0(\beta^{1/2}\xi)$. The equations (A.4)-(A.5) transform into

$$\Phi_{\xi\xi} + \Phi_{\zeta\zeta} = 0, \quad \text{para } 0 < \zeta < 1, \tag{A.6}$$

$$N_t - \Phi_\zeta = 0, \quad \text{en } \zeta = 1, \tag{A.7}$$
$$N + \Phi_t = 0, \quad \text{en } \zeta = 1, \tag{A.8}$$
$$\Phi_\zeta = 0, \quad \text{en } \zeta = 0, \tag{A.9}$$
$$\Phi(\xi,1,0) = \Phi_0(\xi), \quad N(\xi,0) = N_0(\xi), \tag{A.10}$$

and system (A.3) is written as

$$N_t + U_\xi + \frac{1}{2}(Z_0^2 - 1/3)U_{\xi\xi\xi} = 0, \tag{A.11}$$
$$U_t + N_\xi - \frac{1}{2}(Z_0^2 - 1)U_{\xi\xi t} = 0, \tag{A.12}$$
$$U(\xi,0) = F(\xi), \quad N(\xi,0) = N_0(\xi). \tag{A.13}$$

Now let

$$\bar{\omega}^2 = \frac{k^2 - \frac{1}{2}(Z_0^2 - \frac{1}{3})k^4}{1 - \frac{1}{2}(Z_0^2 - 1)k^2} \quad \text{and} \tag{A.14}$$
$$\omega^2 = k\ tanh(k). \tag{A.15}$$

By Fourier transforming the equations above with respect to the spatial variable ξ we obtain the solution of model (A.6)-(A.10) (in the Fourier space)

$$\hat{\phi}(k,\zeta,t) = (D_1(k)e^{i\omega t} + D_2(k)e^{-i\omega t})cosh(k\zeta), \tag{A.16}$$
$$\hat{N}(k,t) = i\omega(-D_1(k)e^{i\omega t} + D_2(k)e^{-i\omega t})cosh(k), \tag{A.17}$$

where

$$D_1(k) = \frac{i\omega\hat{\phi}_0(k) - \hat{N}_0(k)}{2i\omega cosh(k)}, \tag{A.18}$$

$$D_2(k) = \frac{i\omega\hat{\phi}_0(k) + \hat{N}_0(k)}{2i\omega cosh(k)}. \tag{A.19}$$

In order for models (A.6)-(A.10) and (A.11)-(A.13) to coincide at the start ($t = 0$), it is necessary that

$$\hat{\phi}_0(k) = \frac{\hat{F}(k)cosh(k)}{cosh(kZ_0)ki}.$$

By inserting this expression in equations (A.17), we obtain

$$\hat{U}_p(k,t) = \left(\frac{\hat{F}(k)}{2} - \frac{k}{2\omega}\frac{cosh(kZ_0)\hat{N}_0(k)}{cosh(k)}\right)e^{i\omega t} + \left(\frac{\hat{F}(k)}{2} - \frac{k}{2\omega}\frac{cosh(kZ_0)\hat{N}_0(k)}{cosh(k)}\right)e^{-i\omega t}, \tag{A.20}$$

where $\hat{U}_p(k,t) = ik\hat{\phi}(k,Z_0,t)$, i.e. $U_p(\xi,t)$ is the ξ-component of the fluid velocity according to model (A.6)-(A.10). Moreover, the wave elevation can be expressed as

$$\hat{N}_p(k,t) = \left(-\frac{\omega cosh(k)}{2kcosh(kZ_0)}\hat{F}(k) + \frac{1}{2}\hat{N}_0(k)\right)e^{i\omega t} + \left(\frac{\omega cosh(k)}{2kcosh(kZ_0)}\hat{F}(k) + \frac{1}{2}\hat{N}_0(k)\right)e^{-i\omega t}. \tag{A.21}$$

On the other hand, the solution of system (A.11)-(A.13) (in the Fourier space) can be written as

$$\hat{U}(k,t) = \left(\frac{\hat{F}(k)}{2} - \frac{k}{2\bar{\omega}}\frac{\hat{N}_0(k)}{(1-(1/2)(Z_0^2-1)k^2)}\right)e^{i\bar{\omega}t} + \left(\frac{\hat{F}(k)}{2} - \frac{k}{2\bar{\omega}}\frac{\hat{N}_0(k)}{(1-(1/2)(Z_0^2-1)k^2)}\right)e^{-i\bar{\omega}t} \tag{A.22}$$

and

$$\hat{N}(k,t) = \left(-\frac{\bar{\omega}}{2k}\hat{F}(k)(1-(1/2)(Z_0^2-1)k^2) + \frac{1}{2}\hat{N}_0(k)\right)e^{i\bar{\omega}t} + \left(\frac{\bar{\omega}}{2k}\hat{F}(k)(1-(1/2)(Z_0^2-1)k^2) + \frac{1}{2}\hat{N}_0(k)\right)e^{-i\bar{\omega}t}. \tag{A.23}$$

For simplicity, we suppose that the initial data η_0 and f are band limited. Namely, the support of their Fourier transforms are contained in a compact set $[-K,K]$ for some $K > 0$ large enough. Therefore, the support of the Fourier transforms $\hat{N}_0(k)$ and $\hat{F}(k)$ is contained in the interval $[-\sqrt{\beta}K, \sqrt{\beta}K]$.

By expanding the frequencies ω and $\bar{\omega}$ in a Taylor series around $k = 0$, we obtain

$$\omega = k - \frac{1}{6}k^3 + \frac{19}{360}k^5 - \frac{55}{3024}k^7 + O(k^9),$$
$$\bar{\omega} = k - \frac{1}{6}k^3 - \frac{1}{72}(6Z_0^2-5)k^5 - \frac{1}{432}(13-30Z_0^2+18Z_0^4)k^7 + O(k^9).$$

Furthermore

$$\frac{\omega cosh(k)}{2kcosh(kZ_0)} = \frac{1}{2} + \left(\frac{1}{6} - \frac{Z_0^2}{4}\right)k^2 + \frac{1}{720}(4-60Z_0^2+75Z_0^4)k^4 + O(k^6),$$
$$\frac{\bar{\omega}(1-(1/2)(Z_0^2-1)k^2)}{2k} = \frac{1}{2} + \left(\frac{1}{6} - \frac{Z_0^4}{4}\right)k^2 - \frac{1}{144}k^4 + O(k^6).$$

By using these expansions and the equations (A.20)-(A.21) and (A.22)-(A.23) for the Fourier amplitudes, relative to the solution of each model, we obtain the estimate

$$\left|\hat{U}_p(k,t) - \hat{U}(k,t)\right| \leq \hat{F}(k)(O((5Z_0^2-1)tk^5) + O(tk^7)) + \hat{N}_0(k)(O((3-20Z_0^2+25Z_0^4)k^4 + k^6) + O((5Z_0^2-1)tk^5 + tk^7)).$$

Analogously, it follows the estimate

$$\left|\hat{N}_p(k,t) - \hat{N}(k,t)\right| \leq \hat{N}_0(k)(O((5Z_0^2-1)tk^5) + O(tk^7)) + \hat{F}(k)(O((3-20Z_0^2+25Z_0^4)k^4 + k^6) + O((5Z_0^2-1)tk^5 + tk^7)).$$

Thus analyzing the corresponding solutions of models (A.6)-(A.10) and (A.11)-(A.13) in Fourier space, we observe that their smallest difference is achieved when $Z_0 = \sqrt{1/5}$. For this value of the depth parameter, we obtain the following bounds for the velocity and the wave elevation by using the Parseval identity:

$$\|U_p(.,t) - U(.,t)\|_2 \leq \|\eta_0\|_2 (C_1\beta^{15/4} + C_2\beta^{17/4}) + C_3 \|f\|_2 t\beta^{17/4} \tag{A.24}$$

$$\|N_p(.,t) - N(.,t)\|_2 \leq \|f\|_2 (D_1\beta^{15/4} + D_2\beta^{17/4}) + D_3 \|\eta_0\|_2 t\beta^{17/4}, \tag{A.25}$$

where $\|.\|_2$ denotes the L^2 norm and $C_1, C_2, C_3, D_1, D_2, D_3$ are positive constants.

Therefore, the error in the Boussinesq approximation is of $O(\beta^2)$ (both in the wave elevation and the fluid velocity) provided that $0 < t < \beta^{-9/4}$. Note that for β small, say of about 0.01, this gives an extremely large time interval of about 32000 units. This level of accuracy is consistent since the terms neglected in the derivation of system (A.11)-(A.13) (with $\alpha = 0$) are of $O(\beta^2)$.

REFERENCES

[1] Artiles, W. and Nachbin, A. (2004) *Nonlinear evolution of surface gravity waves over highly variable depth*, Phys. Rev. Lett., Vol. 93, 234501.

[2] Artiles, W. and Nachbin, A. (2005) *Asymptotic nonlinear wave modeling through the Dirichlet-to-Neumann operator*, to appear at Methods and Applications of Analysis.

[3] Baines, P.G., (1995) *Topographic Effects in Stratified Flows*. Cambridge: Cambridge Univ. Press.

[4] Berlyand, L. and Burridge, R.(1995) *The accuracy of the O'Doherty-Anstey approximation for wave propagating in highly disordered stratified media*, Wave Motion 21, pp. 357-373.

[5] Bona, J.L. and Chen, H. (1999) *Comparison of model equations for small-amplitude long waves*, Nonlinear Analysis,38, pp. 625-647.

[6] Bona, J.L., Chen, M. and Saut, J.C. (2002) *Boussinesq Equations and other systems for small-amplitude long waves in nonlinear dispersive media. I: Derivation and linear theory.* J. Nonlinear Science, Vol. 12 pp. 283-318.

[7] Burridge, R., Papanicolaou, G.S. and White, B.S. (1988)*One dimensional wave propagation in a highly discontinuous medium*. Wave Motion, 10, pp. 19-44.

[8] Burridge, R. and Chang, H.W. (1989) *Multimode, one-dimensional wave propagation in a highly discontinuous medium*. Wave Motion 11, pp. 231-249.

[9] European Centre for Medium-Range Weather Forecasts (ECMWF) (1998)*Orography*, Proceedings of a Workshop held at ECMWF.

[10] Engquist, B. and Majda, A. (1977)*Absorbing boundary conditions for the numerical simulation of waves*, Math. Comp. 31 (139), pp. 629-651.

[11] Fink, M. (1993) *Time reversal mirrors*, J. Phys. D: Appl. Phys., 26, pp. 1333-1350.

[12] Fouque, J.P. and Nachbin, A. (2003) *Time-reversed refocusing of surface water waves*. SIAM Multiscale Modeling and Simulation, Vol. 1, No. 4, pp. 609-629.

[13] Fouque, J.P., Garnier. J. and Nachbin, A. (2004) *Time reversal for dispersive waves in random media*, SIAM J. Appl. Math. Vol., 64, No. 5, pp. 1810-1838.

[14] Fouque, J.P., Garnier, J. and Nachbin, A. (2004) *Shock structure due to stochastic forcing and the time reversal of nonlinear waves*, Physica D, vol. 195, pp. 324-346.
[15] Fouque, J.P., Garnier, J., Muñoz, J.C. and Nachbin, A.(2004) *Time reversing solitary waves*. Phys. Rev. Lett. 92, No. 9, 094502-1.
[16] Garnier, J. and Nachbin, A. (2004) *The eddy viscosity for time reversing waves in a dissipative environment*, Phys. Rev. Lett., Vol. 93, No. 15, 154501.
[17] Hamilton, J. (1977) *Differential equations for long-period gravity waves on a fluid of rapidly vaying depth*. J. Fluid Mech., 83, pp. 289-310.
[18] Kennedy, A.B., Kirby, J.T., Chen, Q. and Dalrymple, R.A. (2001) *Boussinesq-type equations with improved nonlinear performance*. Wave Motion, 33, pp. 225-243.
[19] Madsen, P.A., Murray, R. and Sørensen, O. R. (1991) *A new form of the Boussinesq equations with improved linear dispersion characteristics (Part1). Coastal Engineering*, 15, pp. 371-388.
[20] Madsen, P.A. and Sørensen, O.R.(1992) *A new form of the Boussinesq equations with improved linear dispersion characteristics, Part 2: A slowly-varying bathymetry*. Coastal Engineering, 18, pp. 183-205.
[21] Matsuno, Y. (1992) *Nonlinear evolution of surface gravity waves on fluid of finite depth*, Phys. Rev. Lett., Vol. 69, No. 4, 609.
[22] Mei, C.C.(1983) *The applied dynamics of ocean surface waves*. Singapore: John Wiley.
[23] Muñoz Grajales, J.C. and Nachbin, A. (2004) *Dispersive wave attenuation due to orographic forcing*. SIAM J. Appl. Math., 64, No. 3, pp. 977-1001.
[24] Muñoz Grajales, J.C. and Nachbin, A.(2005) *Stiff Microscale forcing and solitary wave refocusing*. SIAM Multiscale Modeling and Simulation, Vol. 3, No. 3, pp. 680-705.
[25] Nachbin, A. and Papanicolaou, G.C. (1992) *Water waves in shallow channels of rapidly varying depth*, J. Fluid Mech., Vol. 241, pp. 311–332.
[26] Nachbin, A. (1993) *Modelling of Water Waves in Shallow Channels*. Southampton: Computational Mechanics Publications.
[27] Nachbin, A. (1995) *The localization length of randomly scattered water waves*, J. Fluid Mech., Vol. 296, pp. 353–372.
[28] Nachbin, A. (2003) *A terrain-following Boussinesq system*, SIAM J. Appl. Math., vol. 63, No. 3, pp. 905-922.
[29] Nwogu, O. (1993) *Alternative form of Boussinesq equations for nearshore wave propagation*. J. Waterway, Port, Coastal and Ocean Engineering, 119, pp. 618-638.
[30] Peregrine, D.H. (1967) *Long waves on a beach*, J. Fluid Mech. 27, pp. 815-827.
[31] Pires, C. and Miranda, M.A. (2001) *Tsunami waveform inversion by adjoint methods*, J. Geophys. Res., vol. 106, No. C9, pp. 19733–19796.
[32] Quintero, J.R. and Muñoz Grajales, J.C.(2004) *Existence and uniqueness for a system of Boussinesq equations*. Methods and Applications of Analysis, Vol. 11, No. 1, pp. 15-32.
[33] Schäffer, H.A. and Madsen, P.A. (1995) *Further enhancements of Boussinesq-type equations*. Coastal Engineering, 26, pp. 1-14.
[34] Wei, G. and Kirby, J. (1995) *Time-dependent numerical code for extended Boussinesq equations*, J. of Waterway, Port, Coastal and Ocean Engineering, vol. 121, No. 5, pp. 251-261.
[35] Whitham, G.B. (1974) *Linear and Nonlinear Waves*. New York: John Wiley.
[36] Yoon, S.B. and Liu, P.L.F. (1989) *Interaction of currents and weakly nonlinear waves in shallow water*. J. Fluid Mech., 205, pp. 397-419.